Author/s:
Smith, RA;Castañeda, IS;Groeneveld, J;De Vleeschouwer, D;Henderiks, J;Christensen, BA;Renema, W;Auer, G;Bogus, K;Gallagher, SJ;Fulthorpe, CS

Title:
Plio‐Pleistocene Indonesian Throughflow Variability Drove Eastern Indian Ocean Sea Surface Temperatures

Date:
2020-10

Citation:
Smith, R. A., Castañeda, I. S., Groeneveld, J., De Vleeschouwer, D., Henderiks, J., Christensen, B. A., Renema, W., Auer, G., Bogus, K., Gallagher, S. J. & Fulthorpe, C. S. (2020). Plio‐Pleistocene Indonesian Throughflow Variability Drove Eastern Indian Ocean Sea Surface Temperatures. Paleoceanography and Paleoclimatology, 35 (10), https://doi.org/10.1029/2020pa003872.

Paleoceanography and Paleoclimatology

RESEARCH ARTICLE
10.1029/2020PA003872

Plio-Pleistocene Indonesian Throughflow Variability Drove Eastern Indian Ocean Sea Surface Temperatures

Rebecca A. Smith[1], Isla S. Castañeda[1], Jeroen Groeneveld[2], David De Vleeschouwer[3], Jorijntje Henderiks[4], Beth A. Christensen[5], Willem Renema[6], Gerald Auer[7], Kara Bogus[8,9], Stephen J. Gallagher[10], and Craig S. Fulthorpe[11]

[1]Department of Geosciences, University of Massachusetts Amherst, Amherst, MA, USA, [2]Alfred Wegener Institute, Helmholtz Centre for Polar and Marine Research, Potsdam, Germany, [3]MARUM-Center for Marine and Environmental Sciences, University of Bremen, Bremen, Germany, [4]Department of Earth Sciences, Uppsala University, Uppsala, Sweden, [5]Environmental Science Department, Rowan University, Glassboro, NJ, USA, [6]Nationaal Natuurhistorisch Museum, Leiden, Netherlands, [7]Institute of Earth Sciences, University of Graz, Graz, Austria, [8]Camborne School of Mines, University of Exeter, Penryn, Cornwall, UK, [9]International Ocean Discovery Program, Texas A&M University, College Station, TX, USA, [10]School of Earth Sciences, University of Melbourne, Melbourne, Victoria, Australia, [11]Institute for Geophysics, Jackson School of Geosciences, University of Texas at Austin, Austin, TX, USA

Key Points:
- We provide new sea surface temperature (SST) reconstructions of the Eastern Indian Ocean near the Indonesian Throughflow (ITF) outlet
- Sea surface temperatures near the ITF outlet across the mid-Pliocene Warm Period are up to ~2°C warmer than modern core top values
- The ITF likely underwent restriction that caused a net decrease in Leeuwin Current intensity at ~1.7 Ma

Supporting Information:
- Supporting Information S1
- Table S2
- Table S3
- Table S4
- Table S5

Correspondence to:
R. A. Smith,
rasmith@geo.umass.edu

Citation:
Smith, R. A., Castañeda, I. S., Groeneveld, J., De Vleeschouwer, D., Henderiks, J., Christensen, B. A., et al. (2020). Plio-Pleistocene Indonesian Throughflow variability drove Eastern Indian Ocean sea surface temperatures. *Paleoceanography and Paleoclimatology*, *35*, e2020PA003872. https://doi.org/10.1029/2020PA003872

Received 6 FEB 2020
Accepted 26 SEP 2020
Accepted article online 29 SEP 2020

Abstract Ocean gateways facilitate circulation between ocean basins, thereby impacting global climate. The Indonesian Gateway transports water from the Pacific to the Indian Ocean via the Indonesian Throughflow (ITF) and drives the strength and intensity of the modern Leeuwin Current, which carries warm equatorial waters along the western coast of Australia to higher latitudes. Therefore, ITF dynamics are a vital component of global thermohaline circulation. Plio-Pleistocene changes in ITF behavior and Leeuwin Current intensity remain poorly constrained due to a lack of sedimentary records from regions under its influence. Here, organic geochemical proxies are used to reconstruct sea surface temperatures on the northwest Australian shelf at IODP Site U1463, downstream of the ITF outlet and under the influence of the Leeuwin Current. Our records, based on TEX_{86} and the long-chain diol index, provide insight into past ITF variability (3.5–1.5 Ma) and confirm that sea surface temperature exerted a control on Australian continental hydroclimate. A significant TEX_{86} cooling of ~5°C occurs within the mid-Pliocene Warm Period (3.3–3.1 Ma) suggesting that this interval was characterized by SST fluctuations at Site U1463. A major feature of both the TEX_{86} and long-chain diol index records is a strong cooling from ~1.7 to 1.5 Ma. We suggest that this event reflects a reduction in Leeuwin Current intensity due to a major step in ongoing ITF constriction, accompanied by a switch from South to North Pacific source waters entering the ITF inlet. Our new data suggest that an additional ITF constriction event may have occurred in the Pleistocene.

Plain Language Summary The Indonesian Throughflow (ITF) represents warm water masses flowing from the western Pacific into the Indian Ocean. The ITF flows through the narrow marine passages of the Indonesian Archipelago. This Indonesian Gateway in turn limits the amount of water moving from the Pacific into the Indian Ocean. The depth and width of the Indonesian Gateway has decreased gradually over the past 5 million years due to tectonic movement, which has caused Indonesian islands such as New Guinea and Halmahera to grow and block water entering the Indonesian Archipelago from the warm South Pacific. As a result, most ITF water now derives from the cooler North Pacific, which impacts Indian Ocean temperatures and broader global ocean circulation and heat distribution. The timing of this shallowing of the Indonesian Gateway and transition from warmer South Pacific to cooler North Pacific ITF source waters is not yet fully understood. Here, we present a new sea surface temperature record from near the ITF outlet that shows intense cooling just after 1.7 million years ago. We suggest that this cooling occurred in response to a significant step in the ongoing tectonic constriction and shallowing of the Indonesian Gateway.

1. Introduction

The Indonesian Throughflow (ITF) plays an important role in global thermohaline circulation and significantly influenced Plio-Pleistocene climate (Brierley & Fedorov, 2016; Cane & Molnar, 2001;

De Vleeschouwer et al., 2018; Karas et al., 2009, 2011a, 2011b; Molnar & Cronin, 2015; Sarnthein et al., 2018). However, there are presently few reconstructions of past ITF variability, and no study yet provides high-resolution, multiproxy temperature records of ITF variability extending continuously from 3.5 to 1.5 Ma. Within this interval, the mid-Piacenzian (Pliocene) Warm Period (mPWP; 3.264–3.025 Ma) has been characterized by similar-to-modern atmospheric carbon dioxide (pCO_2) concentrations (Badger et al., 2013; Bartoli et al., 2011; Martínez-Botí et al., 2015; Pagani et al., 2010; Seki et al., 2010; Stap et al., 2016; Zhang et al., 2013) and elevated global surface temperatures relative to preindustrial values (Haywood et al., 2013). As such, it is considered an important, albeit imperfect, analog period for modern and future climate change over the next century (e.g., Burke et al., 2018). To improve climate model configuration and validation, it is critical to identify differences in climate forcing mechanisms such as thermohaline circulation between the modern and mPWP. Therefore, documenting past ITF variability provides climate models with important baseline constraints on changes in thermohaline circulation spanning this highly analyzed warm period.

From 5 to 2 Ma, New Guinea and Australia shifted 2°–3° north, leading to gradual shallowing and progressive constriction of the Indonesian Gateway (Cane & Molnar, 2001). Regional tectonic activity caused the uplift and emergence of the Maritime Continent, located within this gateway, corresponding to an increase in surface area of the modern islands of Indonesia, the Philippines, and Papua New Guinea (Molnar & Cronin, 2015). Cane and Molnar (2001) hypothesized that prior to ~5 Ma, warm, saline South Pacific waters were the source of the ITF into the Indian Ocean (Figure 1). Halmahera Island, part of Indonesia's North Maluku province, has emerged since 5 Myr ago and later grew due to volcanic activity (Cane & Molnar, 2001; Hall et al., 1988). Today it forms a significant land barrier blocking South Pacific waters from entering the ITF (Morey et al., 1999; Figure 1). Cane and Molnar (2001) argue that shallowing and constriction of the Indonesian Gateway, along with the growth of Halmahera, caused a shift to cooler source waters entering the ITF from the North Pacific approximately 3 to 4 Myr ago.

Cane and Molnar's hypothesis was investigated by Karas et al. (2009, 2011a), who reconstructed Indian Ocean Plio-Pleistocene SST and subsurface temperatures using magnesium to calcium (Mg/Ca) ratios of foraminifera. Karas et al. (2009) suggested that the interval from ~3.5 to 2.95 Ma reflects an important step in tectonic reorganization of the Indonesian Gateway, resulting in a switch from South Pacific to North Pacific ITF subsurface source waters reaching central Indian Ocean DSDP (Deep Sea Drilling Program) Site 214 (Figure 1). The authors identified an interval of subsurface cooling at this site by ~4°C from 3.5 to 2.95 Ma, while SST remained constant. Karas et al. (2011a) further hypothesized that tectonic constriction across this interval simultaneously reduced the strength and intensity of the Leeuwin Current reaching ODP (Ocean Drilling Program) Site 763A (Figure 1), which is located offshore western Australia (Figure 1). The authors identified SST cooling at Site 763A from 3.5 to ~3.3 Ma. Today, the relative strength of the Leeuwin Current is largely controlled by the ITF and influences warm water delivery to the Western Australian coast and toward higher latitudes (Feng et al., 2003). It is thought that constriction and shallowing of the Indonesian Gateway in the Pliocene reduced the strength of the ITF and the Leeuwin Current, thereby reducing the amount of warm equatorial Pacific water reaching the northwest coast of Australia (De Vleeschouwer et al., 2019; Gallagher et al., 2009; Song et al., 2007).

We note that both the SST reconstructions of Karas et al. (2009, 2011a) assume a constant seawater Mg/Ca ratio. However, some studies suggest changing seawater Mg concentrations over the past 10 Myr (e.g., Fantle & DePaolo, 2006). If Plio-Pleistocene changes in seawater chemistry influenced foraminiferal Mg/Ca paleothermometry, this could result in underestimates of Pliocene SSTs (Evans et al., 2016; Medina-Elizalde et al., 2008; O'Brien et al., 2014). While the extent of the bias due to long-term changes in Mg/Ca seawater composition is currently debated (e.g., Ford et al., 2015; Medina-Elizalde et al., 2008), additional SST records based on different proxies are necessary for better constraints on Plio-Pleistocene climate change in this region. Furthermore, few long and continuous SST records are available from the Indian Ocean, and additional records are needed to better understand its history and oceanographic processes.

International Ocean Discovery Program (IODP) Expedition 356 cored several sites across the northwest Australian shelf (NWS) with the main objective to better constrain ITF and Leeuwin Current behavior since the Pliocene (Gallagher et al., 2017). Several previous studies from Expedition 356 have investigated past ITF

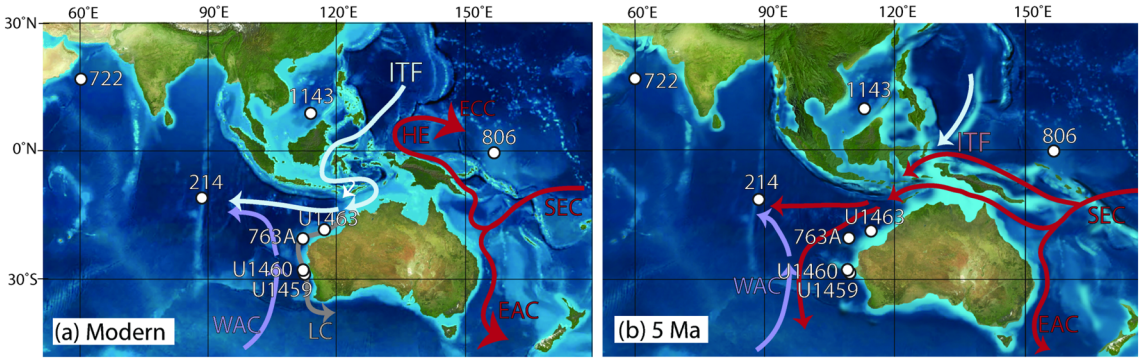

Figure 1. Study location shown with (a) modern ocean currents and (b) with hypothesized Pliocene ocean currents through and around the ITF. HE, Halmahera Eddy; EAC, East Australian Current; ECC, Equatorial Counter Current; SEC, South Equatorial Current; ITF, Indonesian Throughflow; LC, Leeuwin Current; WAC, West Australian Current. Shown in white are IODP Site U1463 (18°58′S, 117°37′E), Perth Basin IODP Sites U1459 (28°40′S, 113°33′E) and U1460 (27°22′S, 112°55′E), central Indian Ocean DSDP Site 214 (11°20′S, 88°43′E; Karas et al., 2009), northwest Arabian Sea ODP Site 722 (16°37′N, 59°48′E; Herbert et al., 2010), South China Sea ODP Site 1143 (9°21′N, 113°17′E), eastern Indian Ocean ODP Site 763A (20°35′S, 112°12′E; Karas et al., 2011a), and equatorial west Pacific ODP Site 806 along the Ontong Java Plateau (0°N, 159°E; Wara et al., 2005). The warmest currents are shown in red, and slightly cooler but still warm equatorial and north Pacific source waters are shown in light blue. SST proxies at Site U1463 likely reflect shifts in LC intensity like those observed at Site 763A, rather than deeper water shifts in ITF source currents from the Pacific as interpreted at Site 214. Base maps sourced from © Colorado Plateau Geosystems, used with permission.

behavior. At IODP Site U1463, Christensen et al. (2017) reconstructed hydrological shifts from 6 to 1 Ma to constrain the timing of northwest Australian hydroclimate response to Plio-Pleistocene ITF variability. Using natural gamma radiation (NGR), the authors identified a humid (5.5 to 3.3 Ma), transition (3.3 to 2.4 Ma), and arid interval (<2.4 Ma) in northwest Australia and hypothesized that these hydrologic shifts were driven by ITF constriction and a switch to North Pacific ITF source waters. At IODP Site U1459, directly under the Leeuwin Current in the Perth Basin (Figure 1), De Vleeschouwer et al. (2019) examined oxygen isotope ($\delta^{18}O$) values of the planktonic foraminifer *Trilobatus sacculifer* and found evidence that tectonic reorganization of the Indonesian Gateway caused a permanent weakening of the Leeuwin Current between 3.7 and 3.6 Ma. Site U1463 (Figure 1), located closer to the ITF outlet, is a more sensitive location to ITF and Leeuwin Current dynamics. At Site U1463, another study of *T. sacculifer* of $\delta^{18}O$ values reports that the ITF constricted by 3.45 Ma (De Vleeschouwer et al., 2018), and a study of calcareous nannofossil assemblage data similarly suggest a switch in ITF source waters occurred at ~3.54 Ma (Auer et al., 2019). Overall, these studies, which utilized different proxies, report variable timing of ITF constriction, but thus far all suggest an important reduction of throughflow and a switch in ITF source waters occurring between 3.5 and 2.95 Ma (Auer et al., 2019; De Vleeschouwer et al., 2018, 2019; Karas et al., 2009, 2011a).

Here, we present the first multiproxy organic geochemical temperature reconstructions from IODP Site U1463 spanning 3.5 to 1.5 Ma. Due to the limited number of SST reconstructions both near the outlet of the ITF and extending into the Pleistocene, the main objective of this research is to further elucidate ITF and Leeuwin Current dynamics across a broad 2 Myr study interval. Results are compared to Mg/Ca-derived SST records from Sites 763A and 214 in order to further evaluate the hypothesis of Cane and Molnar (2001), as well as to Site U1463 NGR data to examine potential relationships between SST and Australian continental aridity (Christensen et al., 2017). Today, a strong correlation between near-shore aridity and offshore Australian SSTs exists (King et al., 2015), and thus, Christensen et al. (2017) emphasized the importance of determining past SST to evaluate relationships with the NGR-derived Australian hydroclimate record. Importantly, to date, most records used to study past ITF variability do not extend beyond 2 Ma (Auer et al., 2019; De Vleeschouwer et al., 2018, 2019; Karas et al., 2009, 2011a) except for one study at Site U1460, located offshore the west coast of Australia, that investigated ITF variability during the past 2.5 Myr (Petrick et al., 2019). Our new SST records from Site U1463, which extend further into the Pleistocene and are from a significantly closer location to the ITF outflow compared to previous investigations, offer new evidence for a possible, and significant, ITF restriction and Indonesian Gateway constriction event between 1.7 and 1.5 Ma.

2. Study Location, Materials, and Methods

2.1. Study Location and Sampling Approach

Site U1463 was cored during IODP Expedition 356 on the NWS (Figure 1) at a present water depth of 145 m, and today lies under the direct path of the modern Leeuwin Current system downstream of the ITF (Gallagher et al., 2017). Pliocene water depths here were up to ~600 m (Gallagher et al., 2017; Gurnis et al., 2020). Site U1463 represents an expanded Plio-Pleistocene section consisting of hemipelagic mud, and foraminiferal assemblages indicate an outer shelf to upper bathyal environment (Gallagher et al., 2017; Gurnis et al., 2020). ITF throughflow is strongest at subsurface depths, notably between 110 and 140 m in the Makassar Strait, the main ITF pathway (Gordon et al., 2008). Our study utilized 376 samples obtained from spliced sections of IODP Holes U1463B and U1463D (Christensen et al., 2017). The sample interval was ~35 cm from 161.45 to 401.77 composite cored meters (CCSF-A) along the splice, with a resolution of one sample per ~5 kyr from 3.48 to 1.50 Ma. Additionally, nine NWS modern (surface) sediment samples that were previously collected during RV SONNE cruise SO257 (Kuhnt et al., 2017) were also analyzed in this study (supporting information Table S1). The IODP Site U1463 age model used here is based on benthic foraminiferal $\delta^{13}C$ and $\delta^{18}O$ of *Uvigerina* spp., as detailed in Groeneveld et al. (2020) (supporting information Figure S1). Spectral analysis on the $\delta^{13}C$ record revealed the presence of the 405-kyr eccentricity record that could be correlated to the global carbon cycles (cycles 5 to 12; Groeneveld et al., 2020; Laskar et al., 2004). The benthic $\delta^{18}O$ record was then used for further tuning the global benthic $\delta^{18}O$ stack LR04 (Lisiecki & Raymo, 2005). The high-resolution expression of glacial-interglacial cycles in the TEX_{86} record presented here was used for fine tuning the latest Pliocene and Pleistocene cycles (Groeneveld et al., 2020). This new age model extends the range of previously published orbital age models for the site on both the older and younger end (Auer et al., 2019; De Vleeschouwer et al., 2018) and increases the temporal resolution and precision of the age model published by Christensen et al. (2017).

2.2. Organic Geochemical Analyses

Samples were freeze dried and homogenized, and total lipid extracts were collected using a Dionex accelerated solvent extractor (ASE 200) and a mixture of dichloromethane (DCM):methanol (MeOH) (9:1, *v*:*v*). Total lipid extracts were dried under N_2 and sequentially separated with alumina oxide into apolar, ketone, and polar fractions using solvent mixtures of DCM:hexane (9:1, *v*:*v*), DCM:hexane (1:1, *v*:*v*), and DCM:MeOH (1:1, *v*:*v*), respectively.

2.2.1. Alkenones

Ketone fractions were analyzed on an Agilent 7890A gas chromatograph (GC) equipped with two flame ionization detectors and Agilent 19091J-416 columns (60 m × 0.32 mm × 0.25 μm) using hydrogen as the carrier gas. The oven program began at 70°C, increased at 17°C min^{-1} to 130°C, then at 7°C min^{-1} to 320°C, and held for 15 min. Alkenone concentrations were quantified using an external squalane calibration curve. The $U^{K'}_{37}$ index is based on the unsaturation ratio of C_{37} long-chain alkenones (Prahl & Wakeham, 1987):

$$U^{K'}_{37} = [C_{37:2}]/[C_{37:2} + C_{37:3}] \quad (1)$$

$U^{K'}_{37}$ values were converted to SSTs using the global core top calibration of Müller et al. (1998), which has a calibration error of ±1.5°C and an upper temperature limit of 29°C:

$$U^{K'}_{37} = 0.033 \times SST + 0.044 \quad (2)$$

2.2.2. Gylcerol Dialkyl Glycerol Tetraethers

Half of each polar fraction was filtered through a 0.45-μm polytetrafluoroethylene filter using hexane:isopropanol (99:1, *v*:*v*), and C_{46} glycerol trialkyl glycerol tetraether (GDGT) was added as an internal standard. GDGTs were measured on an Agilent 1260 series ultrahigh performance liquid chromatograph coupled to an Agilent 6120 single quadrupole mass selective detector following Hopmans et al. (2016). Compounds were eluted from two in series BEH HILIC columns (2.1 × 150 mm, 1.7 μm; Waters®) held initially at 30°C using mixtures of (A) pure hexane and (B) hexane:isopropanol (9:1; *v*/*v*) following the elution method from Hopmans et al. (2016) at a flow rate of 0.2 ml min^{-1}. Isoprenoid GDGTs (iGDGTs) were analyzed in

selective ion monitoring mode for m/z ratios 1,302, 1,300, 1,298, 1,296, 1,292, and 744 (internal standard) to calculate the tetraether index of 86 carbon atoms (TEX_{86}; Schouten et al., 2002):

$$TEX_{86} = \frac{[GDGT-2]+[GDGT-3]+[cren']}{[GDGT-1]+[GDGT-2]+[GDGT-3]+[cren']} \quad (3)$$

where cren′ refers to the crenarchaeol regioisomer. TEX_{86} values were converted to temperature using the SST BAYSPAR (Bayesian, Spatially-Varying Regression) calibration of Tierney and Tingley (2014). The BAYSPAR model accounts for slight deviations from the overall SST-TEX_{86} correlation at a given field location to improve accuracy of TEX_{86} reconstructions by study site (Tierney & Tingley, 2014). The degree of uncertainty is determined within a 5% to 95% confidence interval; regions with abundant surface sediment data have lower bounds of uncertainty (Tierney & Tingley, 2014). However, northwest Australian core top sediments are not currently included in the BAYSPAR calibration or in any global TEX_{86} temperature calibrations; therefore, 5% to 95% uncertainty is high at Site U1463 at about ±5°C to 7°C. Despite this uncertainty, the BAYSPAR calibration yields similar results to both the TEX^{H}_{86} calibration of Kim et al. (2010) and the global TEX_{86} calibration of Kim et al. (2008) (supporting information Figure S2), which have calibration errors of ±1.7°C and ±2.5°C, respectively. The standard error of the Site U1463 TEX_{86} duplicate measurements is ±0.002, or ±0.13°C.

In order to rule out nonthermal effects on TEX_{86}-derived SST, these data were screened using several criteria, including the branched and isoprenoid tetraether (BIT) index (Hopmans et al., 2004), the methane index (MI; Zhang et al., 2011), the GDGT-0/crenarchaeol ratio (Blaga et al., 2009), the ring index (Zhang et al., 2016), and the GDGT-2/GDGT-3 ratio (Taylor et al., 2013).

TEX_{86} values may be influenced by high inputs of soil-derived organic matter because soils and peats contain minor concentrations of iGDGTs (Gattinger et al., 2003; Weijers et al., 2004, 2006), but this influence may be evaluated using the BIT Index (Hopmans et al., 2004).

$$\text{BIT index} = \frac{[\text{brGDGT I} + \text{brGDGT II} + \text{brGDGT III}]}{[\text{brGDGT I} + \text{brGDGT II} + \text{brGDGT III} + \text{IV}]} \quad (4)$$

where brGDGT indicates branched GDGTs. BIT values range from 0 and 1, with values near 0 indicating predominantly marine input and values of 0.98 to 1 indicating predominantly soil origin (Hopmans et al., 2004). BIT values above 0.3 suggest soil inputs of GDGTs, which can affect TEX_{86} derived SSTs (Weijers et al., 2006).

The MI was used to determine the presence of GDGTs derived from methanotrophic Euryarchaeota:

$$MI = \frac{[GDGT-1]+[GDGT-2]+[GDGT-3]}{[GDGT-1]+[GDGT-2]+[GDGT-3]+[\text{crenarchaeol}]+[cren']} \quad (5)$$

Methane index values below 0.3 to 0.4 indicate normal marine conditions suitable for the application of TEX_{86}, while values exceeding 0.5 indicate anaerobic methane oxidation (Zhang et al., 2011). In addition to the MI, the GDGT-0/crenarchaeol (Blaga et al., 2009) ratio was examined because values >2 indicate that the GDGT-0 compound in a sample derives from methanogenic Euryarchaeota.

The ΔRing Index (ΔRI) was determined as an additional proxy for identifying atypical GDGT distributions due to nonthermal factors in sediments (Zhang et al., 2016), where (Equations 6–8)

$$\Delta\text{Ring Index} = RI_{TEX} - RI_{sample} \quad (6)$$

$$RI_{TEX} = -0.77\ (\pm 0.38)\text{x}TEX_{86} + 3.32(\pm 0.34)\text{x}(TEX_{86})^2 + 1.59(\pm 0.10) \quad (7)$$

$$RI_{sample} = 0\text{x}[GDGT-0] + 1\text{x}[GDGT-1] + 2\text{x}[GDGT-2] + 3\text{x}[GDGT-3] + 4\text{x}[Cren] + 4\text{x}[cren'] \quad (8)$$

ΔRI values that exceed 0.3 suggest that TEX_{86} values deviate from modern analogs, and therefore, the associated TEX_{86}-based SSTs are not reliable (Zhang et al., 2015).

Finally, the ratio of GDGT-2/GDGT-3 (Taylor et al., 2013) was calculated in order to determine whether GDGTs originated from Archaea dwelling below or above 1,000-m water depth. A GDGT [2]/[3] > 5 indicates that GDGTs derive from deep-dwelling Archaea (>1,000-m water depth), and TEX_{86} can no longer be utilized for reconstructing SST (Taylor et al., 2013).

2.2.3. Long-Chain Diols

The other half of each polar fraction was derivatized using equal parts of bis(trimethylsilyl)trifluoroacetamide and acetonitrile (1:1, *v:v*) and placed in a 60°C oven for 30 min. Samples were then dried under N_2 gas and injected into an HP 6890 GC coupled to an Agilent 5973 mass selective detector. Compounds were eluted from an Agilent DB-5ms GC column (60 m × 0.32 mm × 0.25 μm) with He as a carrier gas and a temperature program beginning at 70°C, heating to 170°C at 20°C min^{-1}, increasing again to 300°C at 4°C min^{-1}, and remaining at 300°C for 35 min. Compounds were analyzed in selective ion monitoring mode for m/z ratios 299 (C_{28} 1,14 diol), 313 (C_{28} 1,13 and C_{30} 1,15), 327 (C_{30} 1,14), and 341 (C_{30} 1,13 and C_{32} 1,15) to calculate the long-chain diol index (LDI; Equation 9; Rampen et al., 2012):

$$\mathrm{LDI} = \frac{F_{C_{30}1,15-\mathrm{diol}}}{F_{C_{28}1,13-\mathrm{diol}} + F_{C_{30}1,13-\mathrm{diol}} + F_{C_{30}1,15-\mathrm{diol}}} \tag{9}$$

where "*F*" indicates the fractional abundance of each *n*-alkyl diol. LDI values were converted to SST following de Bar et al. (2020). The calibration can estimate SST from −3.3 and 27.4°C and has an error of ±3°C (de Bar et al., 2020):

$$\mathrm{LDI} = 0.0325 \times \mathrm{SST} + 0.1082,\ r^2 = 0.88 \tag{10}$$

While 1,13 and 1,15 *n*-alkyl diols correlate with SST, 1,14 *n*-alkyl diols can be quantified to reconstruct changes in upwelling (Rampen et al., 2008; Willmott et al., 2010). These diols are primarily produced by *Proboscia* diatoms, and have been identified in regions of high primary productivity and upwelling (e.g., Rampen et al., 2008). The diol index (Equation 11; Willmott et al., 2010) was calculated to reconstruct upwelling intensity:

$$\mathrm{Diol\ Index} = \frac{[C_{28} + C_{30}\ 1,14-\mathrm{diols}]}{[(\ C_{28} + C_{30}\ 1,14-\mathit{diol}) + (C_{28} + C_{30}\ 1,13-\mathit{diols})]} \tag{11}$$

Before using the LDI as a SST proxy, it was screened for freshwater diol input by calculating the fractional abundance of the C_{28} 1,12-diol (de Bar et al., 2020):

$$\mathrm{FC}_{28}\ 1,\ 12-\mathrm{diol} = \frac{[\mathrm{C}_{28}\ 1,12-\mathrm{diol}]}{[\mathrm{C}_{28}\ 1,12 + \mathrm{C}_{28}\ 1,13 + \mathrm{C}_{28}\ 1,14 + \mathrm{C}_{30}\ 1,13 + \mathrm{C}_{30}\ 1,14 + \mathrm{C}_{30}\ 1,15-\mathrm{diols}]} \tag{12}$$

The LDI cannot be applied when FC_{28} 1,12-diol >0.1 because of the likely influence of freshwater *Proboscia* diatoms on long-chain diol distribution (de Bar et al., 2020). The fractional abundance of the C_{32} 1,15-diol was also utilized to screen the LDI for freshwater input (Lattaud, Dorhout, et al., 2017). Values of FC_{32} 1,15-diol ≤20 indicate open marine environments (Lattaud, Dorhout, et al., 2017; Lattaud, Kim, et al., 2017). However, de Bar et al. (2020) found that this proxy is only effective in specific regions and encourages the application of both proxies.

3. Results

3.1. Alkenone Ratios and Concentrations

C_{37} and C_{38} alkenones were present in most samples analyzed. $U^{K'}_{37}$ values exhibit high-amplitude variability from 3.5 to 1.5 Ma, ranging from 1.0 (saturation) to 0.42 (supporting information Figure S3). Total C_{37} alkenone concentrations, a commonly used proxy for primary productivity (e.g., Bolton et al., 2010; Lawrence et al., 2006, 2013), are relatively low from 3.5 to 2.3 Ma (Figure 2b) with an average of 1.0 ng C_{37} g sed^{-1} (range: 0.3 to 3.02 ng g sed^{-1}). After ~2.3 Ma, alkenone concentrations increase significantly and become more variable (average: 2 ng C_{37} g sed^{-1}, range: 0.5 to 6.5 ng g sed^{-1}).

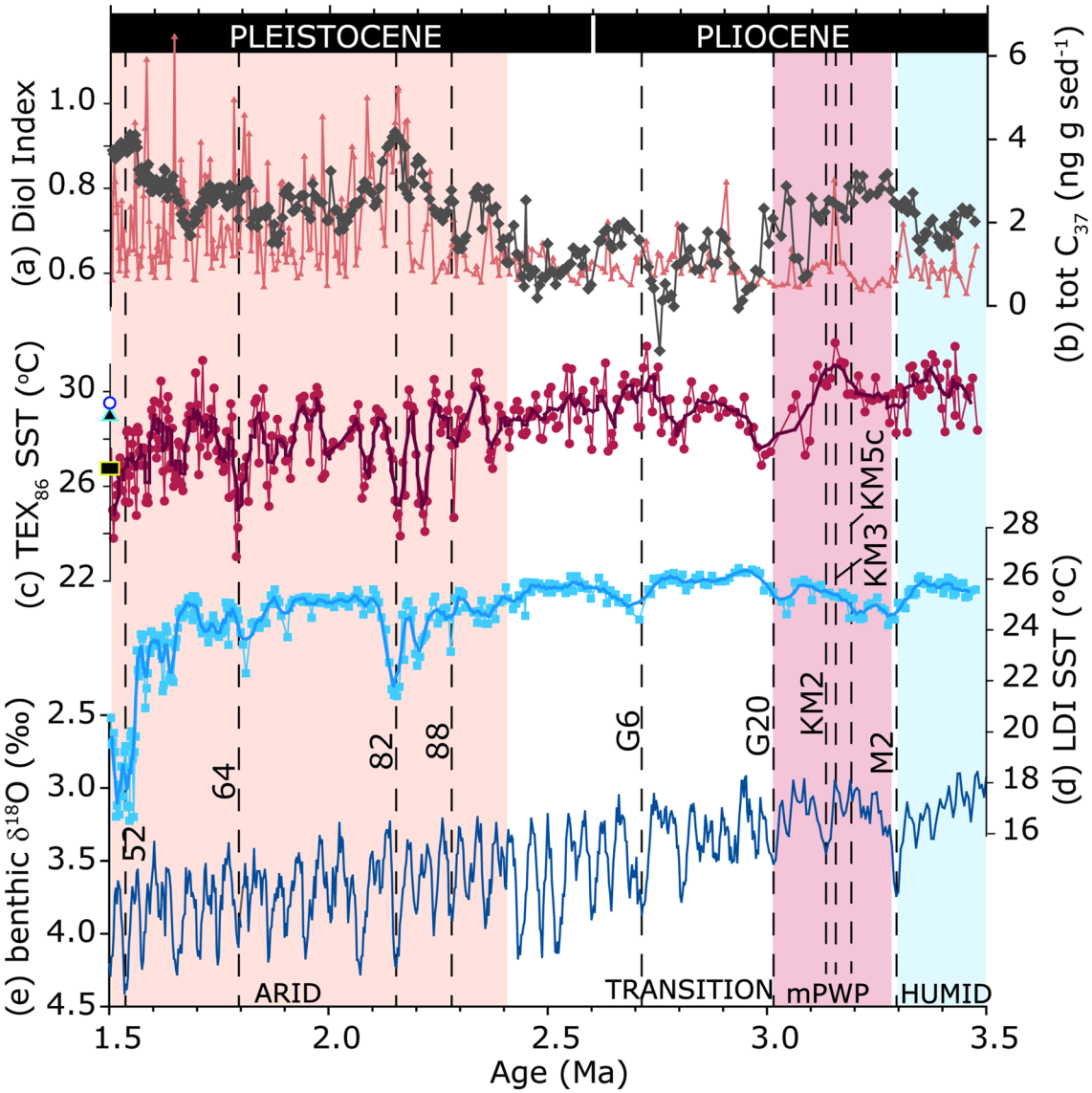

Figure 2. Organic geochemical results from Site U1463 from 3.5 to 1.5 Ma, showing (a) the diol index (gray diamonds) versus (b) total concentrations of C_{37} alkenones (orange triangles), (c) BAYSPAR TEX_{86} SST data (red circles), (d) LDI SST data (blue squares), and the LR04 global benthic $\delta^{18}O$ stack (Lisiecki & Raymo, 2005) is shown (e) to indicate relevant glacial and interglacial periods. Bold lines superimposed on (c) and (d) indicate the 5-point running mean. Along the *y* axis of plot (c), World Ocean Atlas (WOA13) modern mean annual SST (black and yellow square; Locarnini et al., 2013), WOA13 modern summer SST (Locarnini et al., 2013; blue and black diamond), and average TEX_{86}-derived SST from surface sediments is shown (blue and white circle). Dashed lines highlight particularly prominent marine isotope stages (MISs) at Site U1463, namely, MIS 52, 64, 82, 88, G6, G20, KM2, KM3, KM5c, and M2. The humid interval (blue area), transition interval (white and pink area), and arid interval (orange area) are shaded vertically across all data (Christensen et al., 2017). The mPWP (within the transition interval) is highlighted in pink (3.264–3.025 Ma).

The average C_{37}/C_{38} ratio is 2.07 (range: 0.98 to 4.76; supporting information Figure S3). In general, C_{37}/C_{38} values between 0.7 and 1.7 indicate open ocean long-chain alkenone-producing species (Conte et al., 1998; Salacup et al., 2019), which are today dominated by *Emiliana huxleyi* and *Gephyrocapsa oceanica* (Herbert, 2003; Prahl & Wakeham, 1987). In contrast, coastal alkenone-producing haptophytes yield higher values (Ono et al., 2012; Schwab & Sachs, 2011). Therefore, a mean C_{37}/C_{38} value of 2.07 (supporting information Figure S3) suggests the likely presence of coastal haptophyte species. Calcareous nannofossil census data confirm the dominance of small-sized *Reticulofenestra* and *Gephyrocapsa* species (reticulofenestrids) at Sites U1463 and U1464 along the northwest Australian continental shelf margin (Auer et al., 2019; Karatsolis et al., 2020). The reticulofenestrids are the ancestors of *E. huxleyi* and *G. oceanica* and therefore

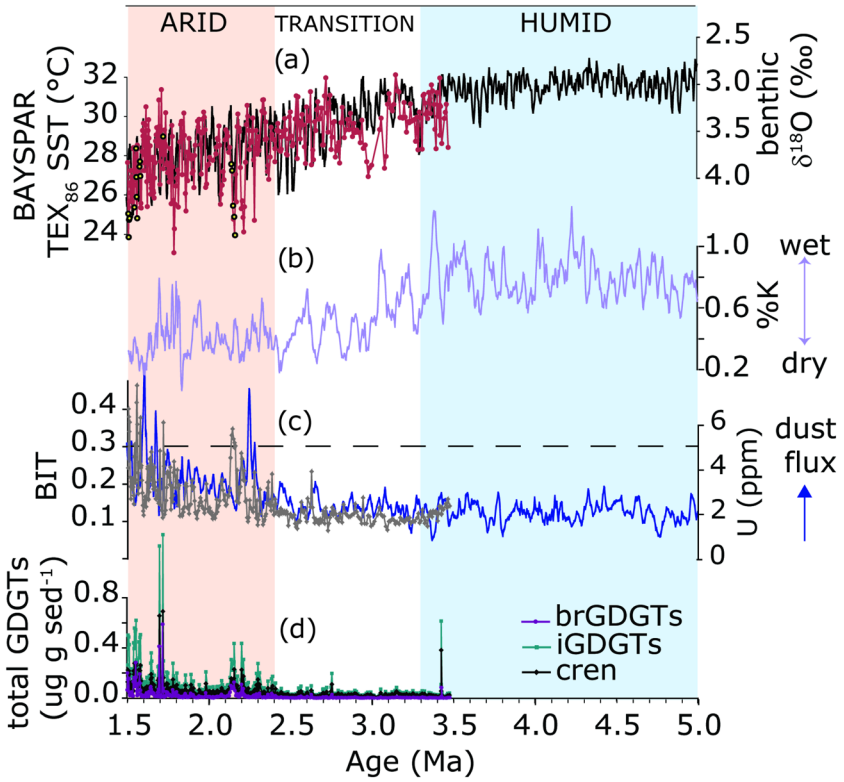

Figure 3. (a) Site U1463 BAYSPAR TEX_{86} SST (red) relative to the LR04 benthic stack (black; Lisiecki & Raymo, 2005), (b) NGR-derived %K from Christensen et al. (2017) (purple), (c) BIT values (gray) relative to NGR-derived U (ppm) from Christensen et al. (2017) (navy), (d) and concentrations of brGDGTs (purple), iGDGTs (teal), and crenarchaeol (black). The humid, transition, and arid intervals identified by Christensen et al. (2017) are shown as blue, white, and orange shaded areas, respectively. Slightly elevated BIT values in the TEX_{86} record are highlighted as yellow and black points in (a), and the BIT threshold is indicated as a dashed line in (c).

the most likely alkenone producers during the investigated time. However, due to the presence of other (but non alkenone-producing) coccolithophore species typical for near-coastal environments, we cannot exclude the existence of additional noncalcifying coastal haptophytes contributing to the alkenone signal or that the reticulofenestrids had "coastal" rather than "oceanic" $U^{K'}_{37}$ signatures. Open ocean and coastal alkenone producing species have different $U^{K'}_{37}$-SST calibrations; therefore, we cannot reliably apply the $U^{K'}_{37}$ SST proxy, as calibrated for the open ocean. Furthermore, values often reach saturation and the Site U1463 $U^{K'}_{37}$ record does not agree with the two other temperature proxies examined here (supporting information Figure S3). Nevertheless, alkenones are sensitive to upwelling because the input of cold, nutrient-rich water triggers primary productivity (Bolton et al., 2010), which allows us to apply total C_{37} alkenone concentrations as a productivity proxy here.

3.2. Screened TEX_{86} Temperatures

Isoprenoid GDGTs are present in all samples, with average concentrations significantly higher (0.11 $\mu g\ g^{-1}$ sediment) than brGDGTs (0.03 $\mu g\ g^{-1}$ sediment) (Figure 3d). The BIT Index ranges between 0.08 and 0.46 (Figure 3c), with an average value of 0.24. The MI values range from 0.18 to 0.36 (supporting information Figure S4) and does not suggest anaerobic methane oxidation here (Zhang et al., 2011). Likewise, the ratio of GDGT-0/crenarcheaol ranges between 0.19 and 0.61 (supporting information Figure S4) and does not point to GDGT-0 in our samples deriving from methanogenic Euryarchaeota (Blaga et al., 2009). The ΔRI exceeds 0.3 (rounded to the nearest decimal) in only 17 of 369 samples, and these outliers (identified in supporting information Figure S4) have been removed from SST reconstructions. Finally, [GDGT-2]/[GDGT-3] values never exceed 2.4 (supporting information Figure S4); therefore, Site U1463 is not influenced by GDGT inputs from deep-dwelling archaea (Taylor et al., 2013).

The TEX_{86} record (Figure 2c) shows overall cooling from 3.5 to 1.5 Ma with SSTs ranging from 23 to 32°C. Large SST decreases (>5°C) occur from 3.2 to 3.0 Ma (~32°C to 27°C), 2.3 to 2.1 Ma (~31°C to 24°C), at 1.8 Ma (~30°C to 23°C), and from 1.7 to 1.5 Ma (~31°C to 24°C). The nine core top samples analyzed across northwest Australia have TEX_{86} values ranging from 0.68 to 0.73, with corresponding BAYSPAR SST (Tierney & Tingley, 2014) estimates of 27.5 to 30.7°C (supporting information Table S1). Hereafter, values from TEX_{86} refer to the BAYSPAR SST calibration unless otherwise stated.

3.3. LDI SSTs

The LDI record (Figure 2d) suggests SSTs of ~23 to 26°C from 3.5 to ~1.7 Ma with several SST minima from ~3.3 to 3.1 Ma, 2.8 to 2.6 Ma, and 2.3 to 2.1 Ma. At 1.8 Ma, SST decreases to ~22°C followed by an increase to ~25°C at 1.7 Ma. Marked cooling occurred from 1.7 to 1.5 Ma, reaching a minimum of ~17°C. The diol index (Figure 2a) resembles the LDI SST trends from ~2.5 to 1.5 Ma, suggesting enhanced upwelling during temperature minima from 2.3 to 2.1 Ma, 1.8 to 1.7 Ma, and 1.7 to 1.5 Ma.

The average diol index from 3.5 to 1.5 Ma is 0.74 and ranges between 0.42 and 0.93 (Figure 2a). We note general agreement between the diol index as an upwelling record and total C_{37} alkenone concentrations as a primary productivity proxy (Figure 2b) (Bolton et al., 2010; Lawrence et al., 2006, 2013).

The fractional abundance of the C_{28} 1,12-diol ranges between 0.155 and 0.005 (supporting information Figure S5). Only nine samples have values ≥0.1, and these were thus omitted from the SST record. The fractional abundance of the C_{32} 1,15-diol is low and never exceeds 7 (supporting information Figure S5).

4. Discussion

4.1. SST Proxy Comparison

4.1.1. TEX_{86}

Several factors should be considered before applying TEX_{86} to reconstruct SST (see also section 3.2). The great majority of U1463 samples have BIT values <0.3, and therefore, TEX_{86} SST are not influenced by soil organic matter inputs at this site. However, a small number of samples (18 of 369) have BIT values >0.3 but never exceed 0.46. Interestingly, the primary increases in BIT at 2.1 Ma and between 1.7 and 1.6 Ma roughly coincide with increases in NGR-derived uranium (U) concentrations (Christensen et al., 2017; Figure 3c). At Site U1463, U serves as a dust proxy due to the presence of U-bearing rocks exposed on the northwest Australian continent (Christensen et al., 2017, and references therein). Therefore, we assume that the slightly elevated BIT values at these times derive from dust, which can carry brGDGTs in low concentrations from continental soils offshore (Fietz et al., 2013; Weijers et al., 2014). Overall, TEX_{86} values at Site U1463 reflect SST due to low BIT values (Figure 3) and for the reasons discussed in section 3.2, but we note that caution should be taken when interpreting SST values for the few samples with slightly elevated BIT values (Figure 3a).

Another consideration when applying TEX_{86} is the fact that iGDGTs are biosynthesized by mesophilic archaea in addition to Thaumarchaeota (Schouten et al., 2002, 2013). Typical Thaumarchaeota in open ocean environments are ammonia-oxidizing Archaea (e.g., Hurley et al., 2016; Schouten et al., 2013, and references therein) and are not restricted to the photic zone. Thus, iGDGTs preserved in Site U1463 sediments may originate from surface or subsurface waters. Prior studies have observed that Thaumarchaeota can occur at mesopelagic and abyssopelagic depths (Karner et al., 2001). Kim et al. (2008) noted a higher correlation between TEX_{86} and epipelagic (<200 m) temperatures than temperatures of deeper water masses (200 to 4,000 m). Within the epipelagic layer, Kim et al. (2008) observed the highest correlation in the mixed layer (upper 30 m), yet other studies have correlated TEX_{86} records to deeper epipelagic (75 to 100 m) GDGT producers (Huguet et al., 2007; Lopes dos Santos et al., 2010; Menzel et al., 2006; Wuchter et al., 2005). At Site U1463 we assume that Thaumarchaeota most likely dwelled within the upper epipelagic region (<100 m). We can rule out GDGT production below 1,000 m since paleodepths likely never exceeded 600 m (Gurnis et al., 2020) and since GDGT-2/GDGT-3 ratios remain below 5 (see section 3.2). Previous studies from southern Australia have concluded that TEX_{86} reflects an upper water column (0 to 200 m) signal (Lopes dos Santos et al., 2013; Smith et al., 2013), while a study of sinking particles offshore Java found that TEX^{H}_{86} reflects an upper thermocline (50 m) water temperature (Chen et al., 2016), in line with our assumptions.

As the global surface sediment data set used for TEX_{86} calibrations lacks samples from the region around Site U1463, we also determined the TEX_{86} of nine core top samples from the northwest Australian shelf to compare with modern SST and subsurface instrumental measurements in the World Ocean Atlas (2013). These samples yield an average TEX_{86}-based SST of 29.5°C (supporting information Table S1). At Site U1463, modern mean annual temperatures are ~27°C at 0 m, ~23°C at 100 m, and ~17°C at 200-m water depth (Locarnini et al., 2013). Therefore, using the BAYSPAR calibration, core top TEX_{86}-based SSTs are 3°C higher than modern mean annual SST. Seasonally, Site U1463 SSTs are ~29°C on average between January and March (summer) and ~25°C between July and September (winter) (Locarnini et al., 2013), suggesting that core top TEX_{86} may reflect austral summer temperature (supporting information Figure S6). We note that the calibration error for BAYSPAR is about ±5 to 7°C, so we cannot conclusively state seasonality of TEX_{86}. Future work using sediment traps, water column filtering, or genetic techniques to determine the dwelling depth and seasonality of Thaumarchaeota offshore northwest Australia is required.

4.1.2. Comparing TEX_{86} and LDI SST Reconstructions

The LDI is a recently developed SST proxy that has been rarely applied to Plio-Pleistocene (Naafs et al., 2012; Plancq et al., 2015) marine strata. Long-chain diols are synthesized by phototrophic diatoms and other types of microalgae (Rampen et al., 2007; Volkman et al., 1992, 1999) living in the photic zone. The LDI can be applied as an SST proxy if diols are not of freshwater origin (de Bar et al., 2020). We identified potential freshwater produced diols in only nine samples, which have been excluded from our records (supporting information Figure S5). Overall, TEX_{86} and LDI (Figure 2d) follow the trends of the global benthic LR04 $\delta^{18}O$ stack (Lisiecki & Raymo, 2005) with higher temperatures in the Pliocene, early stages of cooling beginning at ~3 Ma, and increased Pleistocene cooling after ~1.7 Ma (Figures 2c–2d). Intensified cooling after 1.7 Ma in both records corresponds to the northwest Australian arid interval (Christensen et al., 2017). If considering the relatively large calibration errors for both proxies, LDI and TEX_{86} SST values overlap (supporting information Figure S7). Yet compared to the LDI, TEX_{86} values show more variability from 3.5 to 1.5 Ma and are only weakly correlated with LDI values (supporting information Figure S8). These records correlate better after 2.8 Ma (r = ~0.3–0.7 using 0.5 Ma and 0.25 Ma correlation windows), during a period of more pronounced glacial-interglacial cyclicity in the global benthic stack (Lisiecki & Raymo, 2005) and following the intensification of Northern Hemisphere glaciation (NHG) after 2.7 Ma.

Average LDI-based temperatures of 24.4°C (range: 16.8°C to 26.3°C) are ~4°C lower than average TEX_{86} SSTs of 28.4°C (range: 24.1°C to 32.0°C) from 3.5 to 1.5 Ma (supporting information Figure S7). This difference may be because Site U1463 SSTs approach the upper limit of the LDI proxy. Prior to 2.4 Ma, LDI-SSTs are frequently close to the upper end of the LDI calibration at 27.4°C (de Bar et al., 2020), which may account for the lack of variability compared to TEX_{86} from 3.5 to 2.4 Ma (Figure 2d). Alternatively, the LDI could be influenced by post-depositional oxidation (Reiche et al., 2018; Rodrigo-Gámiz et al., 2016). To date, the few studies that investigated the influence of post-depositional oxidation on LDI have yielded conflicting results. One study found that exposure to oxygen could cause a decrease in LDI and resulting SSTs (Rodrigo-Gámiz et al., 2016). Conversely, a 271-day long aerobic incubation study of *Nannochloropsis oculata* biomass found that LDI values remained stable for the duration of the degradation experiment (Reiche et al., 2018). As our record spans 2 Myr, we speculate that prolonged oxygen exposure, selective organic matter preservation, or other currently unknown chemical, biological, or physical factors influencing degradation of long-chain diols may account for some of the mismatches between the Site U1463 LDI and TEX_{86} records. Oxic degradation likely does not impact isoprenoid TEX_{86} values significantly (Kim et al., 2009; Schouten et al., 2004, 2013). However, neither oxic degradation nor calibration differences likely account for all proxy discrepancies observed at Site U1463. For example, the LDI shows more pronounced cooling than TEX_{86} from 1.7 to 1.5 Ma (Figure 2d), which may be a result of increased upwelling or lateral transport of diols. It seems likely that the former would most convincingly explain this difference because both the diol index and alkenone concentrations suggest upwelling at this time (Figures 2a and 2b).

Seasonal growth biases are another common explanation for differences between SST proxies (Castañeda et al., 2010). When comparing LDI, TEX^{H}_{86}, and $U^{K'}_{37}$ records from southeastern Australia over the past 135 kyr, Lopes dos Santos et al. (2013) concluded that the LDI likely captures austral summer temperatures, whereas TEX^{H}_{86} likely captures a winter signal. Conversely, core top sediments from southeast Australia suggest that LDI reflects winter temperature, while TEX^{H}_{86} reflects 0- to 200-m mean annual temperature

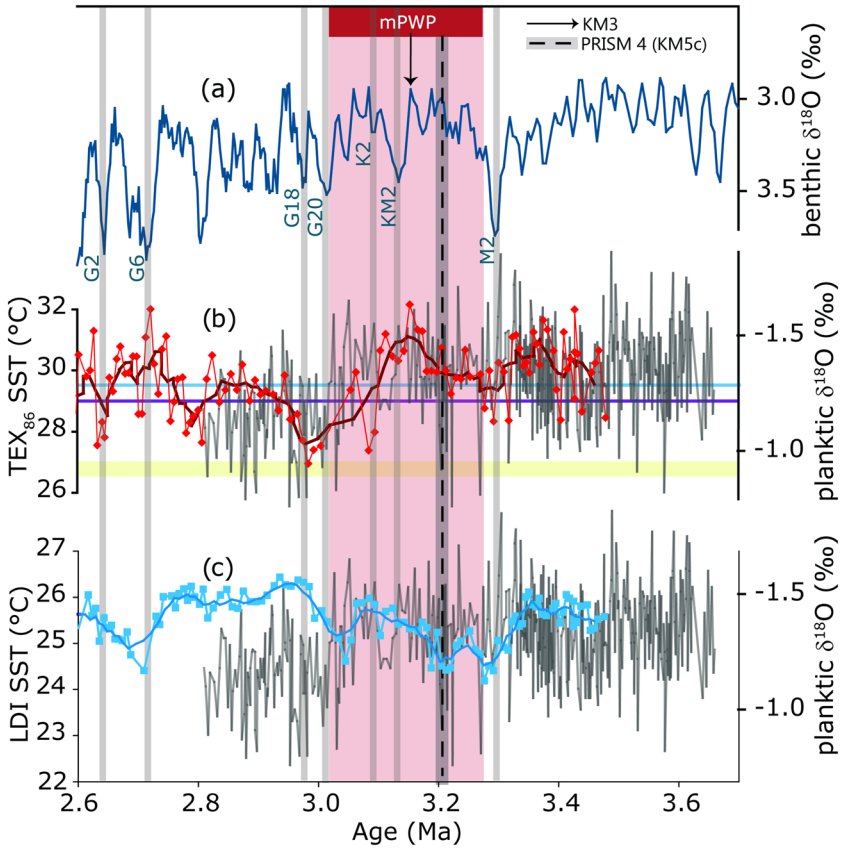

Figure 4. (Comparing Pliocene SST records (TEX_{86} in red and LDI in blue) from Site U1463 to the $\delta^{18}O$ *T. sacculifer* record (gray; De Vleeschouwer et al., 2018). (a) The global benthic LR04 oxygen isotope stack (Lisiecki & Raymo, 2005) (navy) is shown for reference to relevant glacial-interglacial intervals (highlighted as gray bars with individual marine isotope stages numbered). (b) World Ocean Atlas (2013) (WOA13) modern mean annual temperature (yellow horizontal bar) and WOA13 modern summer temperature (purple horizontal line) are shown relative to average core top TEX_{86}-derived SST (blue horizontal line). Both temperature records (b–c) show individual measurements as points and the 5-point running mean in bold. Highlighted in pink is the mPWP, with KM5c shown as a black vertical dashed line and KM3 indicated with a black vertical arrow.

(Smith et al., 2013). Despite our assertion that TEX_{86} may reflect summer temperature at Site U1463 (supporting information Figure S6), we do not attribute the entire temperature offset between proxies to the latter because seasonality can vary over time, and this study extends across a 2-Myr interval at 5-kyr temporal resolution. Furthermore, we cannot rule out the possibility that other nonthermal factors, including differences in light limitation, growth rate, nutrient supply, or other currently unknown factors contributed to the offset between LDI and TEX_{86}-derived temperatures at Site U1463. Despite additional environmental factors that may influence each proxy, it is significant that both records indicate cooling at 1.7 Ma and exhibit broadly similar trends across the study interval. We note that patterns in the Site U1463 TEX_{86} record are in close agreement with the Site U1463 planktonic $\delta^{18}O$ *T. sacculifer* record that is interpreted to reflect SST (De Vleeschouwer et al., 2018; Figure 4b) and broadly agree with the global benthic $\delta^{18}O$ stack (Figure 3a; Lisiecki & Raymo, 2005).

4.2. Plio-Pleistocene SST Variability, ITF History, and Australian Hydroclimate

4.2.1. SST Variability and Aridity in Northwest Australia

Today, offshore SSTs influence Australian near-shore aridity (King et al., 2015); therefore, we utilize Site U1463 SSTs to refine the hydrologic intervals defined by Christensen et al. (2017) and associated with ITF variability since the Pliocene. Christensen et al. (2017) attributed the transition from the humid (5.5 to 3.3 Ma) to transition (3.3 to 2.4 Ma) to arid interval (2.4 Ma to present) with the progressive restriction of the ITF, hypothesizing that a constricted ITF would lower SSTs and reduce net precipitation reaching

northwest Australia. Overall, these hydroclimate shifts (Figures 3b and 3c) coincide with the marked SST changes observed in our records (Figures 2c and 2d), supporting the hypothesis that SST influenced near-shore aridity in Australia during the Plio-Pleistocene (Christensen et al., 2017). Although our records only extend back to 3.5 Ma and therefore do not span the full humid interval, higher temperatures prevailed from 3.5 to 3.3 Ma when northwest Australia likely received year-round precipitation (Christensen et al., 2017). From ~3.0 to 2.4 Ma, relatively stable conditions characterized by lower amplitude temperature fluctuations coincide with the transition interval. However, in the TEX_{86} record a marked SST decrease occurred from ~3.15 to 3.0 Ma, offset from the boundary of the humid and transition interval at 3.3 Ma (Figure 3a; Christensen et al., 2017). The onset of the arid interval is seen in our TEX_{86} record. Starting at 2.4 Ma, the TEX_{86} record exhibits much more variability due to the higher-amplitude glacial-interglacial fluctuations compared to older parts of the record. During the arid interval, the modern northwest Australian dust pathway was established with present-day climate patterns where monsoonal precipitation delivered seasonal moisture. Similar to Christensen et al. (2017), we note a significant change at ~2.4 Ma (Figure 2), well after the intensification of NHG at 2.73 Ma (Haug et al., 1999).

4.2.2. The Mid-Pliocene Warm Period, Marine Isotope Stage M2, and Subsequent Glacials

The mid-Pliocene Warm Period is an important interval for data-model comparisons: It is useful for evaluating the sensitivity of climate under current or future CO_2 levels as well as for evaluating the ability of models to accurately simulate a warm climate (Haywood et al., 2013). A recent study using simulations from six climate models found that under the RCP8.5 emission scenario, Earth will experience a similar climate to the mid–Pliocene by the year 2030 Common Era (Burke et al., 2018).

As expected, our Site U1463 SST records reveal higher temperatures during the Pliocene. From ~3.5 to 3.15 Ma, the Site U1463 TEX_{86} record reveals elevated Pliocene SSTs of up to ~2°C (average of 30.2°C and maximum of 32.1°C) compared to modern core top TEX_{86} temperatures, which range between 27.5 and 30.4°C (supporting information Table S1). This finding is in agreement with both TEX^{H}_{86} (Zhang et al., 2014) and Mg/Ca SST (Wara et al., 2005) estimates from west Pacific Site 806 as well as TEX^{H}_{86} SST from Site U1143 (South China Sea), where even higher temperatures are registered (O'Brien et al., 2014). Thus, our Site U1463 data, proximal to the Western Pacific Warm Pool, support the hypothesis that low-latitude temperatures did not remain stable during the Pliocene and instead were significantly elevated compared to the present (O'Brien et al., 2014). Interestingly, we also observe that Pliocene SSTs were highly variable, especially in the TEX_{86} record (Figure 4), with a dramatic SST drop occurring within the mPWP. From 3.26 to 3.12 Ma (end of MIS M2 through MIS KM2), TEX_{86} SSTs are elevated but subsequently decrease by ~5°C, reaching the lowest values at 3.1 and 3.0 Ma between MIS KM2 and G18 (Figures 4a and 4b). While the mPWP has been regarded as a period of stable climate (Draut et al., 2003), our Site U1463 data (Figure 4b) add to a growing body of evidence questioning that paradigm (e.g., Prescott et al., 2014). Given the current research focus on the mPWP, further studies should regard this interval as a period of high variability, at least at some locations.

Within the generally warm Pliocene, conditions were briefly interrupted by a cooling event associated with MIS M2 (3.312 to 3.264 Ma), the most prominent glacial cycle prior to the intensification of NHG at 2.7 Ma (De Schepper et al., 2014; Lisiecki & Raymo, 2005). MIS M2 has been considered as a "failed attempt" at NHG (Haug & Tiedemann, 1998). De Vleeschouwer et al. (2019) proposed that ITF constriction occurred at ~3.7 Ma, prior to MIS M2, which preconditioned the ITF to experience an extreme sea level lowstand across this glacial interval. They further suggest that low sea level in the ITF region across MIS M2 limited the net volume of water reaching the Indian Ocean from the Pacific, thereby reducing the strength and intensity of the warm Leeuwin Current and decreasing SSTs detected at Site U1463 (De Vleeschouwer et al., 2018). Furthermore, Leeuwin Current weakening would reduce warm water delivery to the Southern Ocean and Antarctica, amplifying glacial conditions across MIS M2 (De Vleeschouwer et al., 2018). The planktonic foraminifer *T. sacculifer* $\delta^{18}O$ values from Site U1463, which were interpreted to reflect temperature, indicate initial warming and subsequent cooling during MIS M2 (Figures 4b and 4c; De Vleeschouwer et al., 2018). Our Site U1463 TEX_{86} record indicates some lower temperatures around MIS M2, although it is not the most pronounced Pliocene cooling event, and the LDI record shows a minor SST fall at this time (Figure 4). The Site U1463 TEX_{86} record generally follows $\delta^{18}O$ trends (Figure 4b). However, we note that the $\delta^{18}O$ record is of significantly higher resolution than the TEX_{86} record and that $\delta^{18}O$ could incorporate salinity as well as temperature.

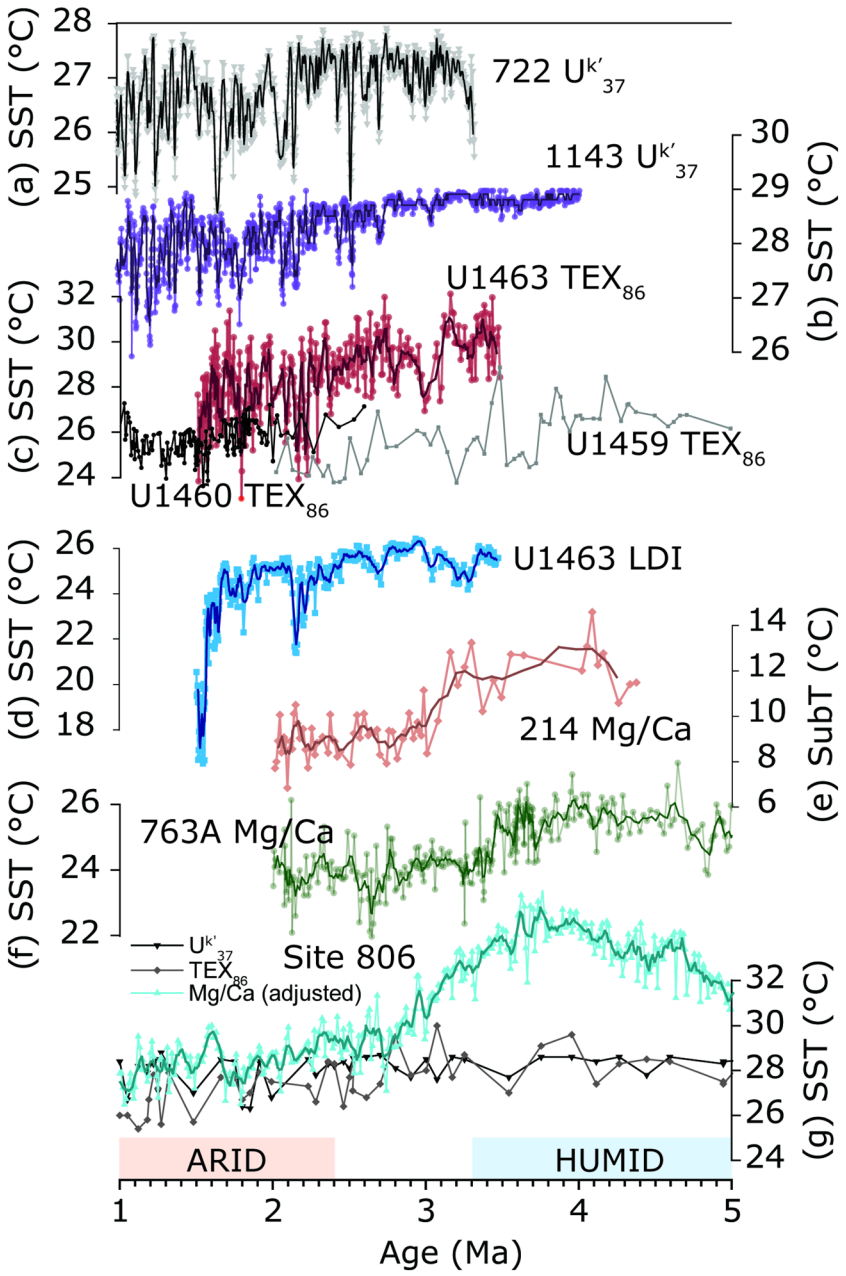

Figure 5. Temperature record comparison from sites surrounding the ITF. (a) Site 722 $U^{K'}_{37}$ SST record (gray triangles; Herbert et al., 2010), (b) Site 1143 $U^{K'}_{37}$ SSTs (purple circles; Li et al., 2011), (c) Site U1463 TEX_{86} SSTs (red circles; this study) and Perth Basin Site U1459 TEX_{86} SSTs (squares; De Vleeschouwer et al., 2019) and Site U1460 TEX_{86} SSTs (black circles; Petrick et al., 2019), (d) Site U1463 LDI SSTs (blue squares; this study), (e) the Site 214 unadjusted Mg/Ca subsurface temperatures (orange diamonds; Karas et al., 2009), (f) Site 763A unadjusted Mg/Ca SSTs (dark green circles; Karas et al., 2011a), and (g) multiproxy SSTs from Site 806. The Site 806 adjusted Mg/Ca record (teal triangles; Medina-Elizalde et al., 2008) is plotted relative to lower resolution TEX_{86} SSTs (gray diamonds) and $U^{K'}_{37}$ SSTs (black triangles; Zhang et al., 2014). Bold lines superimposed on (a) through (g) indicate the 5-point running mean. Shown in blue and orange bars are the humid and arid intervals, respectively, as identified by Christensen et al. (2017).

We observe a slight increase in the diol index beginning just before the onset of MIS M2 (Figure 2a), suggesting an increase in upwelling at Site U1463. Interestingly, Auer et al. (2019) identified a marked reduction in tropical nannofossil abundance at Site U1463 from 3.54 to 3.46 Ma followed by assemblages dominated by opportunistic small reticulofenestrid species with an increase in medium-sized reticulofenestrids during

MIS M2, possibly reflecting higher nutrient availability across this glacial interval. An increase in nutrient availability could be associated with an increase in cold water upwelling at Site U1463. Auer et al. (2019) suggest that a switch in ITF source waters occurred by ~3.54 Ma, refining previous estimates of ITF constriction occurring at 3.5 to 2.95 Ma (Karas et al., 2009, 2011a) and supporting the $\delta^{18}O$ *T. sacculifer* findings by De Vleeschouwer et al. (2018, 2019). Following MIS M2, Auer et al. (2019) documented the occurrence of cooler-water (*Pseudoemiliania*) species (maxima ~4%) during MIS G20, G22, and KM2. The authors hypothesize that ITF constriction and sea level changes associated with MIS M2 triggered the formation of a shallow eastern Indian Ocean thermocline that persisted into the Pleistocene and caused increased sensitivity of the Leeuwin Current to sea level change. Notably, our TEX_{86} data show marked cooling events after MIS M2, particularly during MIS K2 (3.087 to 3.097 Ma) and G18 (2.983 to 2.966 Ma) (Figure 4b). However, these SSTs return to higher values by 2.7 Ma (Figure 2b). Furthermore, diol index values return to low values just after ~3 Ma, suggesting a decrease in upwelling and possibly a weakening of the proposed thermocline at Site U1463. We argue that a permanent constriction would result in a long-term, permanent increase in upwelling as well as a permanent cooling trend in SST associated with the slowing of the Leeuwin Current, which is not observed in the diol index, TEX_{86}, or LDI records (Figure 2).

4.2.3. Timing of ITF Constriction

Our Site U1463 records offer new insights into the timing of ITF constriction, suggesting that tectonically forced ITF constriction continued well after MIS M2 into the Pleistocene. We suggest that these changes occurred in several steps, contributing to the ongoing tectonic reorganization of the Indonesian Gateway since the Pliocene. The previously published ITF studies suggest a major step in tectonic ITF reorganization occurring in the Pliocene between 3.5 and 2.95 Ma (Auer et al., 2019; De Vleeschouwer et al., 2018, 2019; Karas et al., 2009, 2011a). However, these studies did not examine sediments younger than 2 Ma, thereby potentially missing younger significant tectonic or climatically forced changes in Pleistocene ITF dynamics. In the Indian Ocean, the Mg/Ca-derived subsurface and SST record from Site 214 (Figure 5e; Karas et al., 2009) and Site 763A (Figure 5f; Karas et al., 2011a), respectively, indicate significant cooling between 3.5 and 2.95 Ma, suggesting a switch to North Pacific ITF subsurface source waters reaching the central Indian Ocean and net slowing of the Leeuwin Current due to reduced ITF strength. At Site U1463, the TEX_{86} and LDI records show brief cooling intervals beginning at ~3.4 Ma, yet both SST records return to higher values by ~2.7 Ma (Figures 5c and 5d). Therefore, we find that no permanent Leeuwin Current change or shift in ITF source waters is detected at Site U1463 across this interval.

The Site U1463 TEX_{86} and LDI SST records extend the current Indian Ocean SST records further into the Pleistocene, covering the interval from 2.0 to 1.5 Ma near the outlet of the ITF for the first time. Within this interval, both proxies exhibit a strong cooling signal from ~1.7 to 1.5 Ma (Figures 5c and 5d). No large SST cooling signal occurs during this interval at western equatorial Pacific Site 806 (Figure 5g), northwest Indian Ocean Site 722 (Arabian Sea; Herbert et al., 2010), or South China Sea Site 1143 (Li et al., 2011) (Figure 5), all of which are located outside of the direct influence of the ITF (Figure 1). Therefore, the strong cooling at ~1.7 Ma detected at Site U1463 may reflect more a regional, and thus ITF, behavior rather than a global climate signal. Indeed, a TEX_{86} SST record from Site U1460, located off the coast of southwestern Australia and located under the Leeuwin Current influence, suggests ongoing tectonic restriction during the Pleistocene and also displays a significant SST drop at ~1.7 to 1.5 Ma (Petrick et al., 2019; Figure 5c).

Interestingly, ITF constriction at ~1.7 Ma may coincide with changes previously noted in Walker Circulation and African hydroclimate (Lupien et al., 2018; Trauth et al., 2009). If Pleistocene ITF constriction and net cooling of eastern Indian Ocean SSTs at ~1.7 Ma facilitated the formation of a west-east dipping thermocline, as hypothesized by Auer et al. (2019), then the detected cooling along the NWS could have forced changes in African and western Indian Ocean climate via a strengthening of the Sahul-Indian Ocean Bjerknes mechanism (Auer et al., 2019; Di Nezio et al., 2016). Today, a west-east dipping thermocline and cool eastern Indian Ocean SSTs promote a buildup of warm water in the western Indian Ocean and increased convection over East Africa, associated with a positive Indian Ocean Dipole phase (Marchant et al., 2007). Modern modeling studies across interannual timescales suggest a correlation between cool eastern and warm western Indian Ocean SSTs during wet intervals in East Africa (Ummenhofer et al., 2018). Leaf wax carbon ($\delta^{13}C$) and deuterium ($\delta^{2}H$) records from the West Turkana Basin (East Africa) suggest enhanced hydroclimate variability at ~1.73 Ma, possibly associated with the strengthening of Walker Circulation (Lupien et al., 2018). Likewise, Trauth et al. (2007, 2009) suggest that changes in Walker circulation influenced East African hydroclimate

from ~1.9 to 1.7 Ma. Our suggestion of ITF constriction at 1.7 Ma and links to changes in the Walker Circulation requires further testing. In the absence of additional evidence, in the following discussion we also consider changes in global meridional SST gradients, global pCO_2 concentrations, and intensified offshore upwelling as potential mechanisms for cooling at Site U1463.

4.2.4. Changes in Global Climate During Pleistocene Cooling

Changes in atmospheric pCO_2 are a fundamental control on Earth's climate and are thought to have played a role in intensification of glaciations after 2.7 Ma (Bartoli et al., 2011). However, changes in atmospheric pCO_2 are unlikely to account for the rapid SST cooling at ~1.7 Ma at Site U1463. The available global pCO_2 reconstructions do not indicate any rapid decline at this time (supporting information Figure S9). However, these records are too low in resolution to conclusively rule out pCO_2 as a forcing mechanism influencing Site U1463 SSTs across this interval. We note that gradual cooling in TEX_{86} beginning at ~3 Ma (Figure 2) is likely associated with gradual declining pCO_2 concentrations at this time (Badger et al., 2013; Bartoli et al., 2011; Da et al., 2015; Martínez-Botí et al., 2015; Seki et al., 2010; Stap et al., 2016; Zhang et al., 2013).

Another factor that could influence SSTs at Site U1463 is a change in the temperature of the source waters traveling through the ITF due to a change in the heat distribution from the high to low latitudes. Today, higher meridional and zonal SST gradients confine warm waters to the equator. However, during the Pliocene, SSTs were elevated at higher latitudes, and increased ocean temperatures characterized the tropics (Brierley & Fedorov, 2010; Brierley et al., 2009). The progressive constriction of tropical Pacific Ocean water latitudinal extent since the Pliocene (Brierley & Fedorov, 2010; Brierley et al., 2009) likely caused some cooling of North Pacific ITF source water, in turn causing some degree of cooling near the ITF outflow. An increase in global meridional SST gradients was identified when a temperature difference of ~4°C between Eastern Pacific Sites 846 and 1012 (supporting information Figure S9) emerged by 2 Ma (Brierley et al., 2009), just before the onset of marked cooling at 1.7 Ma at Site U1463. Additionally, in the western Pacific closer to the ITF inflow, a meridional SST gradient began to emerge at ~2.8 Ma as temperatures decreased at higher-latitude Site 1208 (LaRiviere et al., 2012) relative to Site 806 (Wara et al., 2005; Zhang et al., 2014; supporting information Figure S9). This increase in the SST difference (ΔSST) between Sites 806 and 1208 approximately coincides with the onset of TEX_{86} cooling at ~3 Ma. Therefore, we suggest that lower SSTs at Site U1463 and an increase in northwest Australian continental aridity after 2.4 Ma (Christensen et al., 2017) may be partly caused by global intensification of meridional gradients and cooling of ITF source waters in the northwestern Pacific. While a change in SST gradients may have been a factor influencing temperatures at Site U1463 between 3 to 2 Ma, the marked cooling events in both the TEX_{86} and LDI records at 1.7 Ma were faster and occurred after the gradual SST gradient shifts in the Pacific. Therefore, gradient changes do not explain the rapid Pleistocene cooling at Site U1463.

It is also possible that strong cooling after 1.7 Ma reflects intensified coastal upwelling at Site U1463. Both total alkenone concentrations and the diol index (Figure 2a) suggest that upwelling increased significantly from 2.3 to 1.5 Ma. Regional upwelling at Site U1463 may be the result of tectonic ITF constriction and slowing of the Leeuwin Current because a net reduction in its intensity would allow for an increase in regional upwelling along the NWS. Offshore western Australia, upwelling via Ekman transport does not occur today because Leeuwin Current flow is typically strong enough to overcome upwelling against the prevailing coastal wind stress (Reason et al., 1999). Alternatively, upwelling at Site U1463 may be related to global changes in primary productivity that occurred at this time. A compilation of 10 Plio-Pleistocene records suggests that time-transgressive productivity declines occurred, with North Atlantic records indicating drops at around 3.3 Ma and more southerly locations experiencing a productivity drop later at ~2.5 Ma (Lawrence et al., 2013). Lawrence et al. (2013) suggest that bihemispheric equatorward shifts in westerly winds caused shifts in Ekman transport and productivity over time. The authors interpret an expanded tropical warm pool above a deep low latitude nutricline, with upwelling and westerly winds at high latitudes prior to 3.3 Ma. During the glacial cycles from 2.7 to 2.5 Ma, there was an equatorward shift of upwelling and westerly wind belts along the Atlantic, and tropical warm pool contraction and the emergence of a shallow nutricline at the equator. Subsequently from 2 to 0 Ma, Lawrence et al. (2013) interpret further equatorward migrations of upwelling and westerly wind belts, a broader nutricline exposure at the equator and increased restriction of warm pool waters. While our upwelling signal at Site U1463 could reflect similar processes to those

described by Lawrence et al. (2013), given its location directly under the Leeuwin Current, we surmise that it is more likely that the upwelling increase from 2.3 to 1.5 Ma reflects a reduction in strength of the Leeuwin Current associated with ITF changes.

In summary, the influence of pCO_2 forcing and meridional and zonal SST gradient changes in the Pleistocene offer possible explanations for cooling at Site U1463 that are unrelated to ITF behavioral changes. However, the rate of cooling we observe in both TEX_{86} and LDI at ~1.7 Ma does not correspond with either pCO_2 forcing or meridional and zonal gradient changes. The recorded changes in both temperature and upwelling most likely reflect a net slowing of the Leeuwin Current associated with tectonic ITF restriction. Furthermore, cooling at ~1.7 to 1.5 Ma is also present in the TEX_{86} record (Figure 1; Petrick et al., 2019) from Site U1460 (Figure 1), off the southwest coast of Australia, indicating that it was not restricted to the NWS. Taken together, these data point to another, and more significant, later stage slowing and cooling of the Leeuwin Current and associated upwelling along the west coast of Australia. We note that as our Site U1463 records end at 1.5 Ma, it is possible that we have not yet fully captured all of the major events associated with ITF constriction and therefore encourage further exploration of ITF behavior spanning the Pleistocene.

5. Conclusions

Our study provides the first multiproxy organic geochemical SST records from Eastern Indian Ocean Site U1463 and thus offers new insights into past environmental variability along the NWS, a region directly influenced by Indonesian Throughflow variability via the Leeuwin Current. Site U1463 SST records display overall trends of Pliocene warmth and cooling into the Pleistocene and also show that Eastern Indian Ocean SST was highly variable during the mPWP. Cooling events after MIS M2 and into the Pleistocene likely resulted from ITF restriction and shallowing of the eastern Indian Ocean thermocline. This caused increased Leeuwin Current sensitivity to sea level fluctuations. While our data offer some support to previous studies suggesting that a step in ITF constriction and a switch in its source waters occurred during the Pliocene between 3.5 and 2.95 Ma, we find little evidence for permanent cooling within this interval. However, we find marked SST cooling occurred at Site U1463 from 1.7 to 1.5 Ma. This cooling event likely reflects another significant step in Leeuwin Current reduction, possibly related to another change in ITF geometry that may have led to a reduction in heat transport from the Western Pacific Warm Pool into the Indian Ocean. Our data extend the history of both the ITF and the Leeuwin Current into the Pleistocene, showing that significant changes in the region occurred later than previously documented.

Acknowledgments

We would like to thank the Editor, the Associate Editor, and three anonymous reviewers for useful feedback, which has significantly strengthened this manuscript. We would like to acknowledge Dr. Jeffrey Salacup, Kathryn Turner, Dr. Sivajini Gilchrist, and Dr. Benjamin Keisling for their help with lab work and sample analyses. This research used samples and data provided by the International Ocean Discovery Program. Funding for organic geochemical analyses was provided by a U.S. Science Support Program (USSSP) Post-Expedition Award to I. S. C. Additional funding was raised through the analysis of external samples at the UMass Amherst Biogeochemistry Laboratory. Funding to S. J. G. was provided by Australian IODP Office and the ARC Basins Genesis Hub (IH130200012). J. G. thanks the German Research Foundation (Deutsche Forschungsgemeinschaft [DFG] Project "IDEAL" GR 3528/5-1). We thank the USIO staff and the SIEM Offshore crew for their invaluable assistance and skill during the expedition.

Data Availability Statement

Data associated with this study are archived at NOAA (https://www.ncdc.noaa.gov/paleo/study/31052) and in Tables S2-S5.

References

Auer, G., De Vleeschouwer, D., Smith, R. A., Bogus, K., Groeneveld, J., Grunert, P., et al. (2019). Timing and pacing of Indonesian Throughflow restriction and its connection to Late Pliocene climate shifts. *Paleoceanography and Paleoclimatology*, *34*, 635–657. https://doi.org/10.1029/2018PA003512

Badger, M. P. S., Schmidt, D. N., Mackensen, A., & Pancost, R. D. (2013). High-resolution alkenone palaeobarometry indicates relatively stable pCO_2 during the Pliocene (3.3–2.8 Ma). *Philosophical Transactions of the Royal Society A: Mathematical, Physical and Engineering Sciences*, *371*(2001), 20130094. https://doi.org/10.1098/rsta.2013.0094

Bartoli, G., Hönisch, B., & Zeebe, R. E. (2011). Atmospheric CO_2 decline during the Pliocene intensification of Northern Hemisphere glaciations. *Paleoceanography*, *26*, PA4213. https://doi.org/10.1029/2010PA002055

Blaga, C. I., Reichart, G.-J., Heiri, O., & Sinninghe Damsté, J. S. (2009). Tetraether membrane lipid distributions in water-column particulate matter and sediments: A study of 47 European lakes along a north–south transect. *Journal of Paleolimnology*, *41*(3), 523–540. https://doi.org/10.1007/s10933-008-9242-2

Bolton, C. T., Lawrence, K. T., Gibbs, S. J., Wilson, P. A., Cleaveland, L. C., & Herbert, T. D. (2010). Glacial–interglacial productivity changes recorded by alkenones and microfossils in late Pliocene eastern equatorial Pacific and Atlantic upwelling zones. *Earth and Planetary Science Letters*, *295*(3–4), 401–411. https://doi.org/10.1016/j.epsl.2010.04.014

Brierley, C. M., & Fedorov, A. V. (2010). Relative importance of meridional and zonal sea surface temperature gradients for the onset of the ice ages and Pliocene-Pleistocene climate evolution. *Paleoceanography*, *25*, PA2214. https://doi.org/10.1029/2009PA001809

Brierley, C. M., & Fedorov, A. V. (2016). Comparing the impacts of Miocene–Pliocene changes in inter-ocean gateways on climate: Central American Seaway, Bering Strait, and Indonesia. *Earth and Planetary Science Letters*, *444*, 116–130. https://doi.org/10.1016/j.epsl.2016.03.010

Brierley, C. M., Fedorov, A. V., Liu, Z., Herbert, T. D., Lawrence, K. T., & LaRiviere, J. P. (2009). Greatly expanded tropical warm pool and weakened Hadley circulation in the early Pliocene. *Science*, *323*(5922), 1714–1718. https://doi.org/10.1126/science.1167625

Burke, K. D., Williams, J. W., Chandler, M. A., Haywood, A. M., Lunt, D. J., & Otto-Bliesner, B. L. (2018). Pliocene and Eocene provide best analogs for near-future climates. *Proceedings of the National Academy of Sciences*, *115*(52), 13,288–13,293. https://doi.org/10.1073/pnas.1809600115

Cane, M. A., & Molnar, P. (2001). Closing of the Indonesian seaway as a precursor to east African aridification around 3–4 million years ago. *Nature*, *411*(6834), 157–162. https://doi.org/10.1038/35075500

Castañeda, I. S., Schefuß, E., Pätzold, J., Sinninghe Damsté, J. S., Weldeab, S., & Schouten, S. (2010). Millennial-scale sea surface temperature changes in the eastern Mediterranean (Nile River Delta region) over the last 27,000 years: Eastern Mediterranean SST records. *Paleoceanography*, *25*, PA1208. https://doi.org/10.1029/2009PA001740

Chen, W., Mohtadi, M., Schefuß, E., & Mollenhauer, G. (2016). Concentrations and abundance ratios of long-chain alkenones and glycerol dialkyl glycerol tetraethers in sinking particles south of Java. *Deep Sea Research Part I: Oceanographic Research Papers*, *112*, 14–24. https://doi.org/10.1016/j.dsr.2016.02.010

Christensen, B. A., Renema, W., Henderiks, J., Vleeschouwer, D. D., Groeneveld, J., Castañeda, I. S., et al. (2017). Indonesian Throughflow drove Australian climate from humid Pliocene to arid Pleistocene. *Geophysical Research Letters*, *44*, 6914–6925. https://doi.org/10.1002/2017GL072977

Conte, M. H., Thompson, A., Lesley, D., & Harris, R. P. (1998). Genetic and physiological influences on the alkenone/alkenoate versus growth temperature relationship in Emiliania huxleyi and Gephyrocapsa oceanica. *Geochimica et Cosmochimica Acta*, *62*(1), 51–68. https://doi.org/10.1016/S0016-7037(97)00327-X

Da, J., Zhang, Y. G., Wang, H., Balsam, W., & Ji, J. (2015). An Early Pleistocene atmospheric CO_2 record based on pedogenic carbonate from the Chinese loess deposits. *Earth and Planetary Science Letters*, *426*, 69–75. https://doi.org/10.1016/j.epsl.2015.05.053

de Bar, M. W., Weiss, G., Yildiz, C., Rampen, S. W., Lattaud, J., Bale, N. J., et al. (2020). Global temperature calibration of the Long chain Diol Index in marine surface sediments. *Organic Geochemistry*, *142*, 103983. https://doi.org/10.1016/j.orggeochem.2020.103983

De Schepper, S., Gibbard, P. L., Salzmann, U., & Ehlers, J. (2014). A global synthesis of the marine and terrestrial evidence for glaciation during the Pliocene Epoch. *Earth-Science Reviews*, *135*, 83–102. https://doi.org/10.1016/j.earscirev.2014.04.003

De Vleeschouwer, D., Auer, G., Smith, R., Bogus, K., Christensen, B., Groeneveld, J., et al. (2018). The amplifying effect of Indonesian Throughflow heat transport on Late Pliocene Southern Hemisphere climate cooling. *Earth and Planetary Science Letters*, *500*, 15–27. https://doi.org/10.1016/j.epsl.2018.07.035

De Vleeschouwer, D., Petrick, B. F., & Martínez-García, A. (2019). Stepwise weakening of the Pliocene Leeuwin Current. *Geophysical Research Letters*, *46*, 8310–8319. https://doi.org/10.1029/2019GL083670

Di Nezio, P. N., Timmermann, A., Tierney, J. E., Jin, F., Otto-Bliesner, B., Rosenbloom, N., et al. (2016). The climate response of the Indo-Pacific warm pool to glacial sea level. *Paleoceanography*, *31*, 866–894. https://doi.org/10.1002/2015PA002890

Draut, A. E., Raymo, M. E., McManus, J. F., & Oppo, D. W. (2003). Climate stability during the Pliocene warm period. *Paleoceanography and Paleoclimatology*, *18*(4), 1078. https://doi.org/10.1029/2003PA000889

Evans, D., Brierley, C., Raymo, M. E., Erez, J., & Müller, W. (2016). Planktic foraminifera shell chemistry response to seawater chemistry: Pliocene–Pleistocene seawater Mg/Ca, temperature and sea level change. *Earth and Planetary Science Letters*, *438*, 139–148. https://doi.org/10.1016/j.epsl.2016.01.013

Fantle, M. S., & DePaolo, D. J. (2006). Sr isotopes and pore fluid chemistry in carbonate sediment of the Ontong Java Plateau: Calcite recrystallization rates and evidence for a rapid rise in seawater Mg over the last 10 million years. *Geochimica et Cosmochimica Acta*, *70*(15), 3883–3904. https://doi.org/10.1016/j.gca.2006.06.009

Feng, M., Meyers, G., Pearce, A., & Wijffels, S. (2003). Annual and interannual variations of the Leeuwin Current at 32°S. *Journal of Geophysical Research*, *108*(C11), 3355. https://doi.org/10.1029/2002JC001763

Fietz, S., Prahl, F. G., Moraleda, N., & Rosell-Melé, A. (2013). Eolian transport of glycerol dialkyl glycerol tetraethers (GDGTs) off northwest Africa. *Organic Geochemistry*, *64*, 112–118. https://doi.org/10.1016/j.orggeochem.2013.09.009

Ford, H. L., Ravelo, A. C., Dekens, P. S., LaRiviere, J. P., & Wara, M. W. (2015). The evolution of the equatorial thermocline and the early Pliocene El Padre mean state. *Geophysical Research Letters*, *42*, 4878–4887. https://doi.org/10.1002/2015GL064215

Gallagher, S. J., Fulthorpe, C. S., Bogus, K., & Expedition 356 Scientists (2017). Proceedings of the International Ocean Discovery Program Volume 356 Expedition Reports. International Ocean Discovery Program College Station, TX, Indonesian Throughflow. https://doi.org/10.14379/iodp.proc.356.2017

Gallagher, S. J., Wallace, M. W., Hoiles, P. W., & Southwood, J. M. (2014). Seismic and stratigraphic evidence for reef expansion and onset of aridity on the Northwest Shelf of Australia during the Pleistocene. *Marine and Petroleum Geology*, *57*, 470–481. https://doi.org/10.1016/j.marpetgeo.2014.06.011

Gallagher, S. J., Wallace, M. W., Li, C. L., Kinna, B., Bye, J. A. T., Akimoto, K., & Torii, M. (2009). Neogene history of the Indo-Pacific Warm Pool, Kuroshio and Leeuwin Currents. *Paleoceanography*, *24*, PA1206. https://doi.org/10.1029/2008PA001660

Gattinger, A., Günthner, A., Schloter, M., & Munch, J. C. (2003). Characterisation of Archaea in soils by polar lipid analysis. *Acta Biotechnologica*, *23*(1), 21–28. https://doi.org/10.1002/abio.200390003

Gordon, A. L., Susanto, R. D., Ffield, A., Huber, B. A., Pranowo, W., & Wirasantosa, S. (2008). Makassar Strait throughflow, 2004 to 2006. *Geophysical Research Letters*, *35*, L24605. https://doi.org/10.1029/2008GL036372

Groeneveld, J., De Vleeschouwer, D., McCaffrey, J., & Gallagher, S. J. (2020). Benthic foraminiferal stable isotopes, planktonic foraminiferal biostratigraphy and seismic profiles for IODP Site 356-U1463. PANGAEA. https://doi.org/10.1594/PANGAEA.921913 (dataset in review)

Gurnis, M., Kominz, M., & Gallagher, S. J. (2020). Reversible subsidence on the North West Shelf of Australia. *Earth and Planetary Science Letters*, *534*, 116070. https://doi.org/10.1016/j.epsl.2020.116070

Hall, R., Audley-Charles, M. G., Banner, F. T., Hidayat, S., & Tobing, S. L. (1988). Late Palaeogene–Quaternary geology of Halmahera, Eastern Indonesia: Initiation of a volcanic island arc. *Journal of the Geological Society*, *145*(4), 577–590. https://doi.org/10.1144/gsjgs.145.4.0577

Haug, G. H., Sigman, D. M., Tiedemann, R., Pedersen, T. F., & Sarnthein, M. (1999). Onset of permanent stratification in the subarctic Pacific Ocean. *Nature*, *401*(6755), 779–782. https://doi.org/10.1038/44550

Haug, G. H., & Tiedemann, R. (1998). Effect of the formation of the Isthmus of Panama on Atlantic Ocean thermohaline circulation. *Nature*, *393*(6686), 673–676. https://doi.org/10.1038/31447

Haywood, A. M., Hill, D. J., Dolan, A. M., Otto-Bliesner, B. L., Bragg, F., Chan, W.-L., et al. (2013). Large-scale features of Pliocene climate: Results from the Pliocene Model Intercomparison Project. *Climate of the Past*, *9*(1), 191–209. https://doi.org/10.5194/cp-9-191-2013

Herbert, T. D. (2003). Alkenone paleotemperature determinations. In *Treatise in Marine Geochemistry* (Vol. 6, pp. 391–432). New York: Elsevier Ltd.

Herbert, T. D., Peterson, L. C., Lawrence, K. T., & Liu, Z. (2010). Tropical ocean temperatures over the past 3.5 million years. *Science*, *328*(5985), 1530–1534. https://doi.org/10.1126/science.1185435

Hopmans, E. C., Schouten, S., & Sinninghe Damsté, J. S. (2016). The effect of improved chromatography on GDGT-based palaeoproxies. *Organic Geochemistry*, *93*, 1–6. https://doi.org/10.1016/j.orggeochem.2015.12.006

Hopmans, E. C., Weijers, J. W. H., Schefuß, E., Herfort, L., Sinninghe Damsté, J. S., & Schouten, S. (2004). A novel proxy for terrestrial organic matter in sediments based on branched and isoprenoid tetraether lipids. *Earth and Planetary Science Letters*, *224*(1–2), 107–116. https://doi.org/10.1016/j.epsl.2004.05.012

Huguet, C., Schimmelmann, A., Thunell, R., Lourens, L. J., Sinninghe Damsté, J. S., & Schouten, S. (2007). A study of the TEX_{86} paleothermometer in the water column and sediments of the Santa Barbara Basin, California. *Paleoceanography*, *22*, PA3203. https://doi.org/10.1029/2006PA001310

Hurley, S. J., Elling, F. J., Könneke, M., Buchwald, C., Wankel, S. D., Santoro, A. E., et al. (2016). Influence of ammonia oxidation rate on thaumarchaeal lipid composition and the TEX_{86} temperature proxy. *Proceedings of the National Academy of Sciences*, *113*(28), 7762–7767. https://doi.org/10.1073/pnas.1518534113

Karas, C., Nürnberg, D., Gupta, A. K., Tiedemann, R., Mohan, K., & Bickert, T. (2009). Mid-Pliocene climate change amplified by a switch in Indonesian subsurface throughflow. *Nature Geoscience*, *2*(6), 434–438. https://doi.org/10.1038/ngeo520

Karas, C., Nürnberg, D., Tiedemann, R., & Garbe-Schönberg, D. (2011a). Pliocene Indonesian Throughflow and Leeuwin Current dynamics: Implications for Indian Ocean polar heat flux. *Paleoceanography*, *26*, PA2217. https://doi.org/10.1029/2010PA001949

Karas, C., Nürnberg, D., Tiedemann, R., & Garbe-Schönberg, D. (2011b). Pliocene climate change of the Southwest Pacific and the impact of ocean gateways. *Earth and Planetary Science Letters*, *301*(1–2), 117–124. https://doi.org/10.1016/j.epsl.2010.10.028

Karatsolis, B., De Vleeschouwer, D., Groeneveld, J., Christensen, B., & Henderiks, J. (2020). The late Miocene–early Pliocene "Humid Interval" on the NW Australian shelf: Disentangling climate forcing from regional basin evolution. *Paleoceanography and Paleoclimatology*, *35*, e2019PA003780. https://doi.org/10.1029/2019PA003780

Karner, M. B., DeLong, E. F., & Karl, D. M. (2001). Archaeal dominance in the mesopelagic zone of the Pacific Ocean. *Nature*, *409*(6819), 507–510. https://doi.org/10.1038/35054051

Kim, J.-H., Huguet, C., Zonneveld, K. A. F., Versteegh, G. J. M., Roeder, W., Sinninghe Damsté, J. S., & Schouten, S. (2009). An experimental field study to test the stability of lipids used for the TEX_{86} and $U_{37}^{K'}$ palaeothermometers. *Geochimica et Cosmochimica Acta*, *73*(10), 2888–2898. https://doi.org/10.1016/j.gca.2009.02.030

Kim, J.-H., Schouten, S., Hopmans, E. C., Donner, B., & Sinninghe Damsté, J. S. (2008). Global sediment core-top calibration of the TEX_{86} paleothermometer in the ocean. *Geochimica et Cosmochimica Acta*, *72*(4), 1154–1173. https://doi.org/10.1016/j.gca.2007.12.010

Kim, J.-H., van der Meer, J., Schouten, S., Helmke, P., Willmott, V., Sangiorgi, F., et al. (2010). New indices and calibrations derived from the distribution of crenarchaeal isoprenoid tetraether lipids: Implications for past sea surface temperature reconstructions. *Geochimica et Cosmochimica Acta*, *74*(16), 4639–4654. https://doi.org/10.1016/j.gca.2010.05.027

King, A. D., Donat, M. G., Alexander, L. V., & Karoly, D. J. (2015). The ENSO-Australian rainfall teleconnection in reanalysis and CMIP5. *Climate Dynamics*, *44*(9–10), 2623–2635. https://doi.org/10.1007/s00382-014-2159-8

Kuhnt, M. W., Holbourn, A. E. L., Schönfeld, J. E. F., & Expedition SO257 Participants (2017). RV SONNE SO257 Cruise report (pp. 1–45). Institute for Geosciences, Kiel Univ. https://www.portal-forschungsschiffe.de/lw_resource/datapool/_items/item_340/03g0257a_20170903_fahrtbericht.pdf

LaRiviere, J. P., Ravelo, A. C., Crimmins, A., Dekens, P. S., Ford, H. L., Lyle, M., & Wara, M. W. (2012). Late Miocene decoupling of oceanic warmth and atmospheric carbon dioxide forcing. *Nature*, *486*(7401), 97–100. https://doi.org/10.1038/nature11200

Laskar, J., Robutel, P., Joutel, F., Gastineau, M., Correia, A., & Levrard, B. (2004). A long-term numerical solution for the insolation quantities of the Earth. *Astronomy & Astrophysics*, *428*(1), 261–285. https://doi.org/10.1051/0004-6361:20041335

Lattaud, J., Dorhout, D., Schulz, H., Castañeda, I. S., Schefuß, E., Sinninghe Damsté, J. S., & Schouten, S. (2017). The C_{32} alkane-1,15-diol as a proxy of late Quaternary riverine input in coastal margins. *Climate of the Past*, *13*(8), 1049–1061. https://doi.org/10.5194/cp-13-1049-2017

Lattaud, J., Kim, J.-H., De Jonge, C., Zell, C., Sinninghe Damsté, J. S., & Schouten, S. (2017). The C_{32} alkane-1,15-diol as a tracer for riverine input in coastal seas. *Geochimica et Cosmochimica Acta*, *202*, 146–158. https://doi.org/10.1016/j.gca.2016.12.030

Lawrence, K. T., Liu, Z., & Herbert, T. D. (2006). Evolution of the eastern tropical Pacific through Plio-Pleistocene glaciation. *Science*, *312*(5770), 79–83. https://doi.org/10.1126/science.1120395

Lawrence, K. T., Sigman, D. M., Herbert, T. D., Riihimaki, C. A., Bolton, C. T., Martinez-Garcia, A., et al. (2013). Time-transgressive North Atlantic productivity changes upon Northern Hemisphere glaciation. *Paleoceanography*, *28*, 740–751. https://doi.org/10.1002/2013PA002546

Li, L., Li, Q., Tian, J., Wang, P., Wang, H., & Liu, Z. (2011). A 4-Ma record of thermal evolution in the tropical western Pacific and its implications on climate change. *Earth and Planetary Science Letters*, *309*(1–2), 10–20. https://doi.org/10.1016/j.epsl.2011.04.016

Lisiecki, L. E., & Raymo, M. E. (2005). A Pliocene-Pleistocene stack of 57 globally distributed benthic $\delta^{18}O$ records. *Paleoceanography*, *20*, PA1003. https://doi.org/10.1029/2004PA001071

Locarnini, R. A., Mishonov, A. V., Antonov, J. I., Boyer, T. P., Garcia, H. E., Baranova, O. K., et al. (2013). World Ocean Atlas 2013. Volume 1, Temperature.

Lopes dos Santos, R. A., Prange, M., Castañeda, I. S., Schefuß, E., Mulitza, S., Schulz, M., et al. (2010). Glacial–interglacial variability in Atlantic meridional overturning circulation and thermocline adjustments in the tropical North Atlantic. *Earth and Planetary Science Letters*, *300*(3–4), 407–414. https://doi.org/10.1016/j.epsl.2010.10.030

Lopes dos Santos, R. A., Spooner, M. I., Barrows, T. T., Deckker, P. D., Sinninghe Damsté, J. S., & Schouten, S. (2013). Comparison of organic ($U^{K'}_{37}$, TEX^{H}_{86}, LDI) and faunal proxies (foraminiferal assemblages) for reconstruction of late Quaternary sea surface temperature variability from offshore southeastern Australia. *Paleoceanography*, *28*, 377–387. https://doi.org/10.1002/palo.20035

Lupien, R. L., Russell, J. M., Feibel, C., Beck, C., Castañeda, I., Deino, A., & Cohen, A. S. (2018). A leaf wax biomarker record of early Pleistocene hydroclimate from West Turkana, Kenya. *Quaternary Science Reviews*, *186*, 225–235. https://doi.org/10.1016/j.quascirev.2018.03.012

Marchant, R., Mumbi, C., Behera, S., & Yamagata, T. (2007). The Indian Ocean dipole? The unsung driver of climatic variability in East Africa. *African Journal of Ecology*, *45*(1), 4–16. https://doi.org/10.1111/j.1365-2028.2006.00707.x

Martínez-Botí, M. A., Foster, G. L., Chalk, T. B., Rohling, E. J., Sexton, P. F., Lunt, D. J., et al. (2015). Plio-Pleistocene climate sensitivity evaluated using high-resolution CO_2 records. *Nature*, *518*(7537), 49–54. https://doi.org/10.1038/nature14145

Medina-Elizalde, M., Lea, D. W., & Fantle, M. S. (2008). Implications of seawater Mg/Ca variability for Plio-Pleistocene tropical climate reconstruction. *Earth and Planetary Science Letters*, *269*(3–4), 585–595. https://doi.org/10.1016/j.epsl.2008.03.014

Menzel, D., Hopmans, E. C., Schouten, S., & Sinninghe Damsté, J. S. (2006). Membrane tetraether lipids of planktonic Crenarchaeota in Pliocene sapropels of the eastern Mediterranean Sea. *Palaeogeography, Palaeoclimatology, Palaeoecology*, *239*(1–2), 1–15. https://doi.org/10.1016/j.palaeo.2006.01.002

Molnar, P., & Cronin, T. W. (2015). Growth of the Maritime Continent and its possible contribution to recurring Ice Ages. *Paleoceanography*, *30*, 196–225. https://doi.org/10.1002/2014PA002752

Morey, S. L., Shriver, J. F., & O'Brien, J. J. (1999). The effects of Halmahera on the Indonesian throughflow. *Journal of Geophysical Research: Oceans*, *104*(C10), 23,281–23,296. https://doi.org/10.1029/1999jc900195

Müller, P. J., Kirst, G., Ruhland, G., von Storch, I., & Rosell-Melé, A. (1998). Calibration of the alkenone paleotemperature index $U^{K'}_{37}$ based on core-tops from the eastern South Atlantic and the global ocean (60°N–60°S). *Geochimica et Cosmochimica Acta*, *62*(10), 1757–1772. https://doi.org/10.1016/S0016-7037(98)00097-0

Naafs, B. D. A., Hefter, J., & Stein, R. (2012). Application of the long chain diol index (LDI) paleothermometer to the early Pleistocene (MIS 96). *Organic Geochemistry*, *49*, 83–85. https://doi.org/10.1016/j.orggeochem.2012.05.011

O'Brien, C. L., Foster, G. L., Martínez-Botí, M. A., Abell, R., Rae, J. W. B., & Pancost, R. D. (2014). High sea surface temperatures in tropical warm pools during the Pliocene. *Nature Geoscience*, *7*(8), 606–611. https://doi.org/10.1038/ngeo2194

Ono, M., Sawada, K., Shiraiwa, Y., & Kubota, M. (2012). Changes in alkenone and alkenoate distributions during acclimatization to salinity change in Isochrysis galbana: Implication for alkenone-based paleosalinity and paleothermometry. *Geochemical Journal*, *46*(3), 235–247. https://doi.org/10.2343/geochemj.2.0203

Pagani, M., Liu, Z., LaRiviere, J., & Ravelo, A. C. (2010). High Earth-system climate sensitivity determined from Pliocene carbon dioxide concentrations. *Nature Geoscience*, *3*(1), 27–30. https://doi.org/10.1038/ngeo724

Petrick, B., Martínez-García, A., Auer, G., Reuning, L., Auderset, A., Deik, H., et al. (2019). Glacial Indonesian Throughflow weakening across the Mid-Pleistocene Climatic Transition. *Scientific Reports*, *9*(1), 16995. https://doi.org/10.1038/s41598-019-53382-0

Plancq, J., Grossi, V., Pittet, B., Huguet, C., Rosell-Melé, A., & Mattioli, E. (2015). Multi-proxy constraints on sapropel formation during the late Pliocene of central Mediterranean (southwest Sicily). *Earth and Planetary Science Letters*, *420*, 30–44. https://doi.org/10.1016/j.epsl.2015.03.031

Prahl, F. G., & Wakeham, S. G. (1987). Calibration of unsaturation patterns in long-chain ketone compositions for palaeotemperature assessment. *Nature*, *330*(6146), 367–369. https://doi.org/10.1038/330367a0

Prescott, C. L., Haywood, A. M., Dolan, A. M., Hunter, S. J., Pope, J. O., & Pickering, S. J. (2014). Assessing orbitally-forced interglacial climate variability during the mid-Pliocene Warm Period. *Earth and Planetary Science Letters*, *400*, 261–271. https://doi.org/10.1016/j.epsl.2014.05.030

Rampen, S. W., Schouten, S., Koning, E., Brummer, G.-J. A., & Sinninghe Damsté, J. S. (2008). A 90 kyr upwelling record from the northwestern Indian Ocean using a novel long-chain diol index. *Earth and Planetary Science Letters*, *276*(1–2), 207–213. https://doi.org/10.1016/j.epsl.2008.09.022

Rampen, S. W., Schouten, S., Wakeham, S. G., & Sinninghe Damsté, J. S. (2007). Seasonal and spatial variation in the sources and fluxes of long chain diols and mid-chain hydroxy methyl alkanoates in the Arabian Sea. *Organic Geochemistry*, *38*(2), 165–179. https://doi.org/10.1016/j.orggeochem.2006.10.008

Rampen, S. W., Willmott, V., Kim, J.-H., Uliana, E., Mollenhauer, G., Schefuß, E., et al. (2012). Long chain 1,13- and 1,15-diols as a potential proxy for palaeotemperature reconstruction. *Geochimica et Cosmochimica Acta*, *84*, 204–216. https://doi.org/10.1016/j.gca.2012.01.024

Reason, C., Gamble, D., & Pearce, A. (1999). The Leeuwin Current in the Parallel Ocean Climate Model and applications to regional meteorology and fisheries. *Meteorological Applications: A Journal of Forecasting, Practical Applications, Training Techniques and Modelling*, *6*(3), 211–225. https://doi.org/10.1017/S1350482799001255

Reiche, S., Rampen, S. W., Dorhout, D. J. C., Sinninghe Damsté, J. S., & Schouten, S. (2018). The impact of oxygen exposure on long-chain alkyl diols and the long chain diol index (LDI)—A long-term incubation study. *Organic Geochemistry*, *124*, 238–246. https://doi.org/10.1016/j.orggeochem.2018.08.003

Rodrigo-Gámiz, M., Rampen, S. W., Schouten, S., & Sinninghe Damsté, J. S. (2016). The impact of oxic degradation on long chain alkyl diol distributions in Arabian Sea surface sediments. *Organic Geochemistry*, *100*, 1–9. https://doi.org/10.1016/j.orggeochem.2016.07.003

Salacup, J. M., Farmer, J. R., Herbert, T. D., & Prell, W. L. (2019). Alkenone paleothermometry in coastal settings: Evaluating the potential for highly resolved time series of sea surface temperature. *Paleoceanography and Paleoclimatology*, *34*, 164–181. https://doi.org/10.1029/2018PA003416

Sarnthein, M., Grunert, P., Khélifi, N., Frank, M., & Nürnberg, D. (2018). Interhemispheric teleconnections: Late Pliocene change in Mediterranean outflow water linked to changes in Indonesian Through-Flow and Atlantic Meridional Overturning Circulation, a review and update. *International Journal of Earth Sciences*, *107*(2), 505–515. https://doi.org/10.1007/s00531-017-1505-6

Schouten, S., Hopmans, E. C., Schefuß, E., & Sinninghe Damsté, J. S. (2002). Distributional variations in marine crenarchaeotal membrane lipids: A new tool for reconstructing ancient sea water temperatures? *Earth and Planetary Science Letters*, *204*(1–2), 265–274. https://doi.org/10.1016/S0012-821X(02)00979-2

Schouten, S., Hopmans, E. C., & Sinninghe Damsté, J. S. (2004). The effect of maturity and depositional redox conditions on archaeal tetraether lipid palaeothermometry. *Organic Geochemistry*, *35*(5), 567–571. https://doi.org/10.1016/j.orggeochem.2004.01.012

Schouten, S., Hopmans, E. C., & Sinninghe Damsté, J. S. (2013). The organic geochemistry of glycerol dialkyl glycerol tetraether lipids: A review. *Organic Geochemistry*, *54*, 19–61. https://doi.org/10.1016/j.orggeochem.2012.09.006

Schwab, V. F., & Sachs, J. P. (2011). Hydrogen isotopes in individual alkenones from the Chesapeake Bay estuary. *Geochimica et Cosmochimica Acta*, *75*(23), 7552–7565. https://doi.org/10.1016/j.gca.2011.09.031

Seki, O., Foster, G. L., Schmidt, D. N., Mackensen, A., Kawamura, K., & Pancost, R. D. (2010). Alkenone and boron-based Pliocene pCO_2 records. *Earth and Planetary Science Letters*, *292*(1–2), 201–211. https://doi.org/10.1016/j.epsl.2010.01.037

Smith, M., De Deckker, P., Rogers, J., Brocks, J., Hope, J., Schmidt, S., et al. (2013). Comparison of $U^{K'}_{37}$, TEX^{H}_{86} and LDI temperature proxies for reconstruction of south-east Australian ocean temperatures. *Organic Geochemistry*, *64*, 94–104. https://doi.org/10.1016/j.orggeochem.2013.08.015

Song, Q., Vecchi, G. A., & Rosati, A. J. (2007). The role of the Indonesian Throughflow in the Indo–Pacific climate variability in the GFDL Coupled Climate Model. *Journal of Climate*, *20*(11), 2434–2451. https://doi.org/10.1175/JCLI4133.1

Stap, L. B., de Boer, B., Ziegler, M., Bintanja, R., Lourens, L. J., & van de Wal, R. S. W. (2016). CO_2 over the past 5 million years: Continuous simulation and new δ^{11}B-based proxy data. *Earth and Planetary Science Letters*, *439*, 1–10. https://doi.org/10.1016/j.epsl.2016.01.022

Taylor, K. W. R., Huber, M., Hollis, C. J., Hernandez-Sanchez, M. T., & Pancost, R. D. (2013). Re-evaluating modern and Palaeogene GDGT distributions: Implications for SST reconstructions. *Global and Planetary Change*, *108*, 158–174. https://doi.org/10.1016/j.gloplacha.2013.06.011

Tierney, J. E., & Tingley, M. P. (2014). A Bayesian, spatially-varying calibration model for the TEX_{86} proxy. *Geochimica et Cosmochimica Acta*, *127*, 83–106. https://doi.org/10.1016/j.gca.2013.11.026

Trauth, M. H., Larrasoaña, J. C., & Mudelsee, M. (2009). Trends, rhythms and events in Plio-Pleistocene African climate. *Quaternary Science Reviews*, *28*(5–6), 399–411. https://doi.org/10.1016/j.quascirev.2008.11.003

Trauth, M. H., Maslin, M. A., Deino, A. L., Strecker, M. R., Bergner, A. G. N., & Dühnforth, M. (2007). High- and low-latitude forcing of Plio-Pleistocene East African climate and human evolution. *Journal of Human Evolution*, *53*(5), 475–486. https://doi.org/10.1016/j.jhevol.2006.12.009

Ummenhofer, C. C., Kulüke, M., & Tierney, J. E. (2018). Extremes in East African hydroclimate and links to Indo-Pacific variability on interannual to decadal timescales. *Climate Dynamics*, *50*(7–8), 2971–2991. https://doi.org/10.1007/s00382-017-3786-7

Volkman, J. K., Barrett, S. M., & Blackburn, S. I. (1999). Eustigmatophyte microalgae are potential sources of C_{29} sterols, C_{22}–C_{28} n-alcohols and C_{28}–C_{32} n-alkyl diols in freshwater environments. *Organic Geochemistry*, *30*(5), 307–318. https://doi.org/10.1016/S0146-6380(99)00009-1

Volkman, J. K., Barrett, S. M., Dunstan, G. A., & Jeffrey, S. W. (1992). C_{30}-C_{32} alkyl diols and unsaturated alcohols in microalgae of the class Eustigmatophyceae. *Organic Geochemistry*, *18*(1), 131–138. https://doi.org/10.1016/0146-6380(92)90150-V

Wara, M. W., Ravelo, A. C., & Delaney, M. L. (2005). Permanent El Nino-like conditions during the Pliocene Warm Period. *Science*, *309*(5735), 758–761. https://doi.org/10.1126/science.1112596

Weijers, J. W. H., Schefuß, E., Kim, J.-H., Sinninghe Damsté, J. S., & Schouten, S. (2014). Constraints on the sources of branched tetraether membrane lipids in distal marine sediments. *Organic Geochemistry*, *72*, 14–22. https://doi.org/10.1016/j.orggeochem.2014.04.011

Weijers, J. W. H., Schouten, S., Spaargaren, O. C., & Sinninghe Damsté, J. S. (2006). Occurrence and distribution of tetraether membrane lipids in soils: Implications for the use of the TEX_{86} proxy and the BIT index. *Organic Geochemistry*, *37*(12), 1680–1693. https://doi.org/10.1016/j.orggeochem.2006.07.018

Weijers, J. W. H., Schouten, S., van der Linden, M., van Geel, B., & Sinninghe Damsté, J. S. (2004). Water table related variations in the abundance of intact archaeal membrane lipids in a Swedish peat bog. *FEMS Microbiology Letters*, *239*(1), 51–56. https://doi.org/10.1016/j.femsle.2004.08.012

Willmott, V., Rampen, S. W., Domack, E., Canals, M., Sinninghe Damsté, J. S., & Schouten, S. (2010). Holocene changes in Proboscia diatom productivity in shelf waters of the north-western Antarctic Peninsula. *Antarctic Science*, *22*(01), 3–10. https://doi.org/10.1017/S095410200999037X

Wuchter, C., Schouten, S., Wakeham, S. G., & Sinninghe Damsté, J. S. (2005). Temporal and spatial variation in tetraether membrane lipids of marine Crenarchaeota in particulate organic matter: Implications for TEX_{86} paleothermometry. *Paleoceanography*, *20*, PA3013. https://doi.org/10.1029/2004PA001110

Zhang, Y., Pagani, M., Liu, Z., Bohaty, S., & DeConto, R. (2013). A 40-million-year history of atmospheric CO_2. *Philosophy*, *371*, 10–1098.

Zhang, Y. G., Pagani, M., & Liu, Z. (2014). A 12-million-year temperature history of the tropical Pacific Ocean. *Science*, *344*(6179), 84–87. https://doi.org/10.1126/science.1246172

Zhang, Y. G., Pagani, M., & Wang, Z. (2016). Ring Index: A new strategy to evaluate the integrity of TEX_{86} paleothermometry. *Paleoceanography*, *31*, 220–232. https://doi.org/10.1002/2015PA002848

Zhang, Y. G., Zhang, C. L., Liu, X.-L., Li, L., Hinrichs, K.-U., & Noakes, J. E. (2011). Methane Index: A tetraether archaeal lipid biomarker indicator for detecting the instability of marine gas hydrates. *Earth and Planetary Science Letters*, *307*(3–4), 525–534. https://doi.org/10.1016/j.epsl.2011.05.031